Heuristic Data-inspired Scheme to Characterize Meteorological and Groundwater Droughts in Semi-arid Karstic Region under Warming Climate

Hakan Başağaoğlu[a,*], Chetan Sharma[b], Debaditya Chakraborty[b,**], Icen Yoosefdoost[b], F. Paul Bertetti[a]

[a] *Edwards Aquifer Authority, 900 E. Quincy St., San Antonio, TX, USA 78215*
[b] *School of Civil and Environmental Engineering, and Construction Management, University of Texas at San Antonio, One UTSA Circle, San Antonio, TX, USA 78249*

Abstract

Study region

The Edwards Aquifer Region is located in south-central Texas, United States.

Study focus

The paper focuses on the development and implementation of a data-inspired heuristic drought identification scheme to (i) quantify the intensity, duration, and frequency of precipitation deficit- and high temperature-driven meteorological droughts (PMet- and TMet-droughts), and (ii) link their propagation to groundwater droughts (GW-droughts) using baseline hydroclimatic measures and prevailing drought conditions derived from historical climate data and regional mitigation strategies.

*corresponding author: hbasagaoglu@edwardsaquifer.org
**corresponding author: debaditya.chakraborty@utsa.edu

New hydrological insights for the region

Based on the intensity, duration, and timing of PMet- and TMet-droughts in the semi-arid karstic region, we identified three distinct GW-droughts, including persistence-driven, preconditions-driven, and intensity-driven droughts. The analysis revealed that successive heavy precipitation events are needed to end GW-droughts in the region. The scheme also identified TMet-droughts with the longest dry spells, TMet- and PMet-droughts with the highest intensity, and GW-drought with the second-highest intensity on record all occurred over the past 15 years. These findings provide evidence for a warming climate, intensified meteorological droughts, and increasing stress on the aquifer. Among the artificial intelligence models used, Extremely Randomized Trees (ERT) predicted time series of intensity & duration of GW-droughts from hydroclimatic features with high accuracy. Moreover, the ERT classifier revealed that the duration of PMet droughts and the intensity of TMet droughts are the topmost decisive features in predicting GW-drought intensity in the region.

Keywords: Meteorological drought, Groundwater drought, Semi-arid karstic region, Warming climate, Successive heavy precipitation events

---

1. Introduction

Drought is a recurrent and disruptive component of hydroclimatic variability that can arise from sustained precipitation deficits in conjunction with elevated temperatures over an extended period of time [1, 2]. Prolonged high temperatures and lack of precipitation (meteorological drought) could increase potential evapotranspiration while lowering soil moisture, groundwater recharge, and storage of surface and subsurface water resources (hydrological drought). As a consequence of soil moisture deficit and water scarcity, vegetation growth and crop yield could be reduced (agricultural drought). This could subsequently exert increasing stress on water and food security, natural capital, and economic welfare (socioeconomic drought) [1, 3] as well as on the sustainability of ecologically-sensitive groundwater-dependent habitats (ecological drought) [4].

Groundwater drought, as part of hydrological drought, is the main focus of this paper. It depends not only on meteorological factors (e.g., elevated temperature and precipitation deficit) [5, 6] but also on dynamic interactions of climate and terrestrial components (e.g., altered land cover as a result of deforestation and overfarming) [2] and overexploitation of groundwater resources [7]. During groundwater drought, aquifer recharge, groundwater yields, capillary rise, and spring flows and sustainability of groundwater-dependent ecosystems are adversely affected [8, 9]. Assessment and prediction groundwater drought particularly in karstic systems are challenging due to the complex flow patterns involving slow seepage through the rock matrix and fast flow through solutionally enlarged conduits, heterogeneous and anisotropic hydrogeologic properties, and limited understanding of hydraulics [10, 11], which could be even more challenging under changing climate. Therefore, robust and reliable methods to identify meteorological and groundwater droughts and examine the cause-effect relationship are needed. Such analyses are imperative for forewarning future droughts using projected climate data from global climate models and the development of mitigation strategies for sustainable and climate-resilient groundwater operations.

Using local meteorological, regional atmospheric, and climatic variables, the Effective Drought Index (EDI) [12], Standardized Precipitation Index (SPI) [13], Standardized Precipitation Evaporation Index (SPEI) [14], Standardized Streamflow Index (SSI) [15], and Standardized Groundwater Index (SGI) [16] have been used to analyze meteorological and hydrological droughts at various spatial-scales covering different climatic regimes. SPI and SGI were used together to estimate the duration and severity of meteorological and groundwater droughts [17, 18]. However, due to complex nonlinear relationships among hydroclimatic variables controlling droughts [19], drought indices may not perform well at all locations and hydroclimatic conditions, and hence, cannot be used universally as a robust tool for drought risk assessment and forecast [20, 21]. In addition, the analysis of drought with indices such as SPI can be contentious because the Gamma distribution, used in SPI to fit precipitation, may poorly represent precipitation patterns that are likely better described by Generalized Extreme Value or Generalized Logistic distributions [22]. Notably, the uncertainty and error associated with such indices for the evaluation of drought severity have been reported to be significant [23].

Alternative methods proposed in the literature to quantify droughts and drought propagation involve empirical [24], physics-based, conceptual, statistical [25], stochastic [26], probabilistic [27], or AI-based models such as artificial neural networks [28], support vector machines [29], decision trees [30], or hybrid models that combine these different models [31]. Empirical models are simple but are unable to capture nonlinear relationships among hydroclimatic variables. The main challenge in physics-based models is appropriate accounting for the uncertainties associated with input data, model calibration, and numerical scheme that would have direct impacts on the drought quantification [1, 32]. When probabilistic models are used for drought analyses, verification of model accuracy for large complex systems could be challenging [33]. On the other hand, nonlinear multivariate problems, like those encountered in drought analyses, are well-suited to AI-based models. Complex hydrogeologic properties and strong nonlinearity between input an output variables are more pronounced in karstic aquifer systems that involve intricate features such as dissolution-enlarged fractures, heterogeneous conduit flows, sinkholes, and sinking streams [34–36]. Therefore, AI-based models would be inherently instrumental in assessing drought risks in karstic systems. Until now, AI-based models, however, have been commonly used as a black-box model in predicting index-based drought risk analyses without implementing explanatory methods for enhanced explainability of the results. When combined with explanatory methods such as SHaply Additive exPlanation (SHAP) [37, 38], AI-based models can be used to justify decision making and discover new knowledge [39, 40].

Due to the absence of a universally accepted method for the assessment of meteorologic and groundwater droughts and drought propagation in the literature, the main motivation of this study is to establish a heuristic data-driven scheme to characterize meteorological and groundwater droughts and disclose the nature of drought propagation using long-term daily hydroclimatic data. Different from the earlier drought risk assessments, we aim to quantify the intensity, duration, and frequency of temperature- and precipitation deficit-driven meteorological droughts separately as either one could be the main driver [41, 42] but account for their joint impacts on the intensity and duration of groundwater droughts. Few studies reported drought analysis for karstic aquifers; however, they were limited to assessing the effects on water quality and hydrogeology [43, 44]. In addition, drought propagation analyses for large karstic aquifer systems available in the literature have typically focused on exploring the relationship between SPI and groundwater drought [45, 46]. The use of such relationships, however, is often ineffective in the assessment or forecasting of groundwater drought in karst aquifer systems because SPI and groundwater droughts are commonly asynchronous [47]. Thus, the need for the use of data-driven approaches with long-term observed records in the assessment of groundwater droughts has been emphasized in the literature [48, 49].

The main objectives of this paper are to (i) establish data-driven baseline measures to define deviations from 'normal' hydrologic conditions [1] and prevailing drought conditions to determine the intensity, duration, and frequency of meteorologic and groundwater droughts in a karstic semi-arid region, and (ii) assess the AI-based predictability of groundwater drought intensity from the meteorologic drought features and hydroclimatic data. To accomplish these objectives, we focus on the following research questions: (i) What are the proper baseline measures, dry spells, and prevailing conditions for meteorological and groundwater droughts in the semi-arid karstic region? (ii) What are the interplay and combined roles of high temperature- and precipitation deficit-driven meteorological droughts on groundwater droughts? (iii) Can groundwater droughts be differentiated based on the intensity, duration, and timing of meteorological droughts? (iv) Would severe storms (i.e., the right tail of a precipitation distribution) and/or high precipitation deficits (i.e., the left tail of a precipitation distribution) be pivotal in assessing the severity or termination of groundwater droughts? (v) Would the intensity of groundwater drought be predictable from the intensity and duration of high temperature- or precipitation deficit-driven meteorological droughts? and (vi) Can the effect of a warming climate on the intensity and duration of local meteorological and groundwater droughts be untangled? Using current hydroclimatic data, our method would be capable of quantifying the intensity and duration of a new drought event in comparison to past droughts, which is important for the development of climate-resilient drought mitigation strategies. The scheme can also be used to predict potential future groundwater droughts from meteorological conditions based on projected downscaled climate data from global climate models.

2. Materials and Methods

In Section 2.1, we described the study region that overlies a prolific karstic aquifer home to endemic endangered and threatened groundwater-bound species. Using mitigation measures that have been enforced in the study region since the 2000s to protect the aquifer and vulnerable aquatic species (Section 2.2) and daily hydroclimatic data since the 1940s (Section 2.3), we introduced in Section 2.4 a drought-intensity calculation scheme using site-specific baseline measures for meteorological and groundwater droughts. In the same section, we also explained how the duration and frequency of droughts were computed. We described in Section 2.5 how the baseline measures and prevailing conditions for droughts were established.

Next, we formulated new explainable artificial intelligence (XAI) models to test the predictability of historical groundwater droughts from historical hydroclimatic data. For this purpose, we integrated AI regressors (Section 2.6) with a post hoc explainability method called SHAP (Section 2.7), forming an XAI model, to identify the most critical hydroclimatic features in predicting the intensity of historical groundwater droughts. Additionally, we integrated AI classifiers with SHAP (Section 2.7) to reveal the relative importance of the intensity and duration of historical high temperature- and low precipitation-driven meteorological droughts in predicting the intensity of historical groundwater droughts.This information is crucial to unveil how meteorological droughts propagate into groundwater droughts in the region.

2.1. Study region

The Edwards Aquifer in semi-arid south-central Texas, United States (Fig. 1) is one of the world's most species-rich prolific karstic aquifer and is home to threatened and endangered endemic aquatic species [50, 51]. The aquifer is the primary source of drinking water for the city of San Antonio and the surrounding region with a population of over 2 million. It is also the source of water for recreational, ranching, irrigation, and industrial uses in the region.

The aquifer thickness ranges from about 137m to 335m. The aquifer is highly heterogeneous and anisotropic with hydraulic conductivity and transmissivity varying over eight orders of magnitude regionally, but it is highly transmissible in the confined or Artesian Zone with transmissivities ranging from about 40,000 to 200,000 m^2/d [36, 52]. It contains a variety of highly permeable dissolution features (e.g., sinkholes, caves), fracture networks, and conduit flow zones, whose hydrogeological characteristics have been significantly impacted by structural features such as faulting and uplifting. Further information on the hydrogeologic and karstic characteristics of the aquifer along with the representative stratigraphic column and cross-sections can be found in [36].

Flow within the aquifer is from higher to lower elevations and generally west to east, where the aquifer has major natural discharge points at the Comal and San Marcos springs systems. Flow magnitude and direction are significantly impacted by faulting, and a series of structural features in the

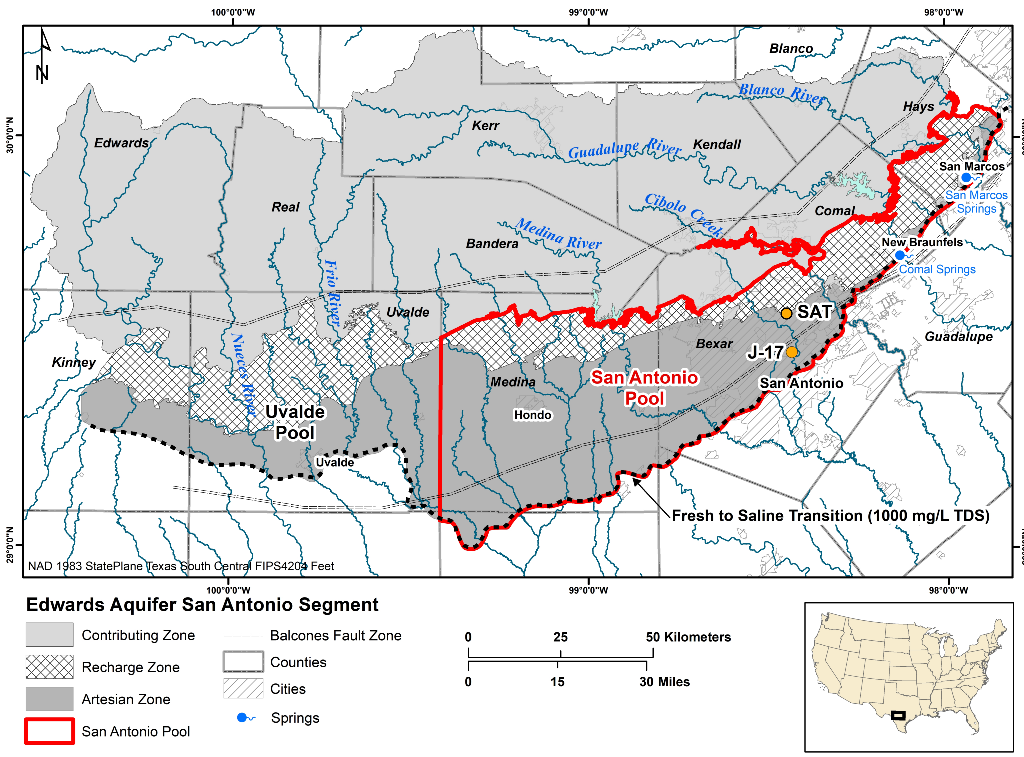

Figure 1: The map shows the semi-arid Edwards Aquifer Region under the jurisdiction of the Edwards Aquifer Authority. Groundwater levels at the J-17 index well (J-17) trigger mandated reductions in groundwater withdrawals to offset the adverse impacts of droughts on groundwater levels and habitats of the endangered and threatened aquatic species in the Comal and San Marcos springs. The San Antonio International Airport (SAT) has the longest meteorological records in the region. Total area of the Edwards Aquifer Region including Contributing Zone is 22,800 km^2. The area of Recharge and Artesian zones combined is 8,550 km^2 and the area of the San Antonio Pool is 5,600 km^2.

.

Artesian Zone in the western portion of the aquifer form a hydraulic restriction to flow from west to east in that area. This restriction is known locally as the Knippa Gap and is located approximately along the reach of the Frio River in Uvalde County. The hydraulic behavior of the aquifer is different across this restriction—the Uvalde Pool in the west has semi-confined characteristics while the San Antonio Pool to the east is primarily a confined system, and the Pools are managed separately to account for this difference [53]. To make regulatory management clearer, the San Antonio Pool extent is arbitrarily defined at the boundary between Uvalde and Medina counties even though the physical barrier is a few kilometers to the west of the boundary. The San Antonio Pool accounts for about two-thirds of the areal extent of the aquifer. In this study, we focus on the San Antonio Pool of the Edwards Aquifer Region.

The Edwards Aquifer Region experienced the most severe historic drought from 1949 through 1957, which is often referred to as the 'Drought of Record'. The 1950s drought was caused by high temperature (Fig. 2a-b) and low precipitation (Fig. 2c) (meteorological drought). During this period, groundwater levels (GWL) at the J-17 index well dropped to historically low levels (Fig. 2d) due to close to zero estimated aquifer recharge, which caused the ecologically vulnerable Comal Springs to run dry for four months in 1956 (hydrological drought) [54]. Historical data reveal that groundwater levels and spring flows in the Edwards Aquifer Region are vulnerable to meteorological droughts.

2.2. Critical period management strategies

Critical Period Management (CPM) strategies are part of the mitigation strategies in the San Antonio Pool to protect the aquifer and groundwater-fed aquatic habitats. They have been in effect since 2002 and consist of five

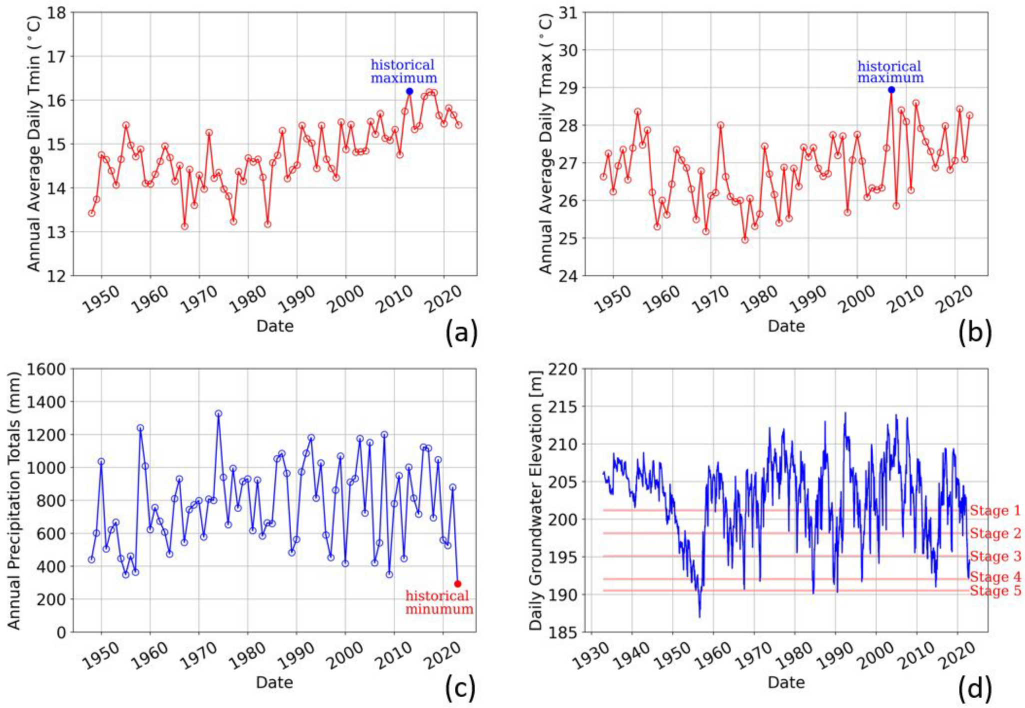

Figure 2: Annual-averaged daily minimum (T_{min}) (a) and maximum temperatures (T_{max}) (b), and annual total precipitation (P) (c) at the San Antonio International Airport (SAT), and 10-day rolling-averaged daily groundwater level (GWL_{RA-10d}) at the J-17 index well (d). Increasing trends in T_{min} and T_{max} since the 1980s are indications of a warming climate at the airport location. Although P shows fluctuations with no prevailing trend, the annual P total was the lowest on record (since the 1940s) at the airport area in 2022. The Critical Period Management, as part of the regional mitigation measures, has been implemented since 2002, and the associated critical stages (Table 1) are shown on the historical groundwater level data in (d). Persistent declines in groundwater levels occurred during the 1950s (1949 - 1957), 2010s (2011-2015), and 2022 droughts when precipitation was low and temperature was high. Intermittent groundwater droughts in the mid-1980s and early and mid-1990s can also be observed from these plots.

stages [51]. The stages delineate reductions in permitted groundwater withdrawals when groundwater levels drop below-specified values within the San Antonio Pool to ensure the sustainability of Edwards Aquifer's groundwater and safeguard habitats of groundwater-bound threatened and endangered species in San Marcos and Comal springs during drought periods (Table 1)

[51]. The annual permitted pumping across the Edwards Aquifer region prior to any stage restrictions are limited to 730.78 million m^3/yr.

Table 1: Critical Period Management (CPM) program triggers, stages, and pumping reductions associated with groundwater levels (GWL) at the J-17 index well for the San Antonio Pool of the Edwards Aquifer system.

	Critical Period Stage 1	Critical Period Stage 2	Critical Period Stage 3	Critical Period Stage 4	Critical Period Stage 5
GWL(m)*	<201	<198	<195	<192	<190.5
GWL(m)†	<33.7	<19.15	<8.65	<3.0	<0.9
Reduction	20%	30%	35%	40%	44%

* 10-day rolling-averaged values (msl)
† CPM stages are expressed in terms of the percentile of historical GWL(m)

2.3. Datasets

For the drought analysis, historical climate data, including daily maximum temperatures (T_{max}) and daily total precipitation (P) recorded at the SAT from 1946 to 2023, encompassing the 1950s drought, were acquired from the National Oceanic and Atmospheric Administration's integrated surface database. The daily historical groundwater level data at the J-17 index well from 1934 to 2023 were obtained from the Edwards Aquifer Authority. Although the karstic Edwards Aquifer is highly heterogeneous, groundwater level at the J-17 well is representative of spatiotemporal variations in groundwater levels in the San Antonio Pool of the aquifer, and hence, have been used as an index well for managing groundwater operations within the Pool since 2002. Similarly, historical P and T_{max} data reveal that meteorological data at the SAT are representative of the climatic conditions in the San Antonio

Pool. Representativeness of the climate data at the SAT and groundwater level data at the J-17 index well for the San Antonio Pool of the aquifer is elaborated in Appendix A. 10-day rolling-averaged GWL (GWL_{RA-10d}) and T_{max} (T_{RA-10d}) and 10-day rolling-summed P (P_{RS-10d}) were used in our analyses to smooth-out potential noise in the data.

As for groundwater pumping, the total permitted annual groundwater pumping across the Edwards Aquifer Region is capped at 730.38 m^3/yr. Additional pumping restrictions are enforced when groundwater levels fall below the critical stages in Table 1. The amount of exempt or non-permitted pumping is %$3-5$ of the total average annual withdrawals and approximately 2% of the permitted pumping cap, and hence, it has relatively small impacts on the aquifer system. Permitted pumping wells have been metered since the early 2000s. Therefore, groundwater pumping data prior to 2000 were generated from inverse modeling of groundwater levels and spring flows using numerical simulations, but the calibrated pumping data have inherently large uncertainties, therefore the pumping data has not been used in our data-driven XAI analysis. As a result, we exclusively focused on the effects of the more accurately measured daily T_{max}, P, and GWL in quantifying the intensity, drought, and frequency of droughts in the region.

2.4. Intensity, duration, frequency calculations

The intensity of meteorological and groundwater droughts is computed by modifying the equation in [55] as follows:

$$I = \frac{\sum_k \phi\left(x_k - \chi\right)}{D}; k \in [i, j] \tag{1}$$

where x is GWL_{RA-10d}, or T_{RA-10d}, or P_{RS-10d}, i and j are the start and end of a drought event, D is the duration of a drought event, and ϕ =-1 when x is used for GWL or P, whereas ϕ =1 when x is used for T_{max}. χ is the site-specific baseline measure defined separately for GWL_{RA-10d}, T_{RA-10d}, and P_{RS-10d}. The numerator in Eq. 1 represents the total deficit below (for GW- and PMet-droughts) or above (TMet-drought) the baseline level [56]. Duration (D) is determined by how long the T_{max} continuously exceeded the baseline temperature and how long GWL or P persistently remained below its corresponding baseline measures during droughts. The frequency (F) describes the number of occurrences of a drought event with a calculated intensity in a prescribed range over the entire time period. Determination of the baseline T_{max}, P, and GWL, and the conditions describing the commencement and pervasiveness of dry spells are the key aspects of drought assessments, while the intensity-duration-frequency are the key metrics to characterize droughts.

2.5. Baseline measures and prevailing conditions for droughts

2.5.1. Groundwater droughts

According to the CPM triggers in Table 1, when GWL_{RA-10d} at the J-17 index well drops below 201 m, CPM-stage 1 is initiated and results in a mandated 20% reduction in permitted groundwater pumping within the Edwards

Aquifer Authority's jurisdiction of the San Antonio Pool of the aquifer. More significant restrictions are enacted through CMIP-stage 5, which is triggered when GWL_{RA-10d} drops below 190.5 m and mandates a 44% reduction in permitted withdrawals. Therefore, we set the baseline GWL to CPM-stage 1 to flag the start of potential groundwater drought when GWL drops below 201 m. We define the prevailing condition for groundwater drought (GW-drought, hereafter) when GWL_{RA-10d} remains persistently below CPM-stage 1 for at least 3 months (>90 days). Departure from 'normal' hydrological conditions for at least 3 consecutive months was used as a drought identification criterion in earlier studies [57].

2.5.2. High temperature-driven meteorological droughts

The National Weather Service describes extreme heat events as heatwaves if daily $T_{max} \geq 32°\text{C}$ for 3 consecutive days or more [58, 59]. Short-term heatwaves may not cause drought, but prolonged and hotter heatwaves could lead to drought conditions or exacerbate ongoing drought [60] . Therefore, we set the baseline $T_{max} = 32°\text{C}$. To be consistent with the GW-drought condition, we define the necessary condition for high temperature-driven meteorological drought (TMet-drought, hereafter) such that if T_{RA-10d} persistently exceeds 32°C for at least 3 consecutive months, the corresponding dry spell is deemed to be associated with TMet-drought.

2.5.3. Precipitation deficit-driven meteorological droughts

In recent precipitation deficit-driven meteorological drought (PMet- drought, hereafter) analyses, months with 3-month rolling-averaged P totals (P_{RA-3m}) below the 15$^{\text{th}}$ percentile of P_{RA-3m} were considered to be drought [55]. When we applied this meteorological drought definition to the 1950s (1949 - 1957) and 2010s (2011-2015) droughts, it failed to accurately represent PMet-droughts in relation to GW-droughts, as most of the dry months were inaccurately identified as non-drought (Fig. B.1).

A mismatch between PMet-droughts computed by the conceptualization in [55] and GW-droughts can be attributed to the consideration of the left tail of a precipitation distribution (P_{LT}) without considering the role and effect of the right tail of a precipitation distribution (P_{RT}) in GW-drought assessments. The timing, magnitude, and successiveness of P_{RT}, however, would be the decisive factors for GW-drought duration if aquifer recharge is contributed largely by focused recharge rather than diffuse recharge. Focused recharge is associated with discrete features (e.g., sinkholes) and dissolution along faults and fractures exposed within ephemeral and perennial stream channels. These features are typical of the geomorphology of a karstic region. The focused recharge contribution to aquifer recharge increases during severe storms. Diffuse recharge, on the other hand, is associated with gravity-driven distributed recharge over inter-stream areas and is more vulnerable to evapotranspiration in semi-arid regions. In the Edwards Aquifer Region, focused recharge has been estimated to account for $\sim$70% of the total aquifer recharge [61], suggesting that the frequency and intensity of severe storms, represented by P_{RT}, would be the key determinant for the duration and intensity of GW-droughts. We tested this conjecture using P_{RS-10d} for the 1950s and 2010s GW-droughts and P_{RT} defined as

$$P_{RT} = P_{\mu,RS-10d} + P_{n\sigma,RS-10d}, \tag{2}$$

where $P_{\mu,RS-10d}$ and $P_{n\sigma,RS-10d}$ are the mean (μ) and n$^{\text{th}}$ standard deviations (σ) of the mean of P_{RA-10d}. n=3 was found to capture persistent PMet-droughts associated with GW-droughts in the 1950s and 2010s reasonably well while accurately representing non-groundwater drought periods in 1972-1980 and 2003-2010, as shown in Fig. B.2.

According to Eq. 2, PMet-drought associated with GW-drought would end when $P_{RA-10d} > P_{RT}$ in successive storm events. As shown in Fig. 2d, GWL_{RA-10d} were at the historically lowest levels over the period of 1949–1957. The 1950s GW-drought ended following successive P_{RT} storms in 1957 and 1958 that increased the focused recharge and aquifer recovery (Fig. 3a). Similarly, successive P_{RT} storms in 2015 forbore the 2010s GW-drought. Based on the historical data, we conceptualize that PMet-drought would propagate to GW-drought when $P_{RA-10d} < P_{RT}$ is persistent for at least 12 months. The 12-month period is in agreement with the 12-month time-scale used with the SPI (SPI12) in [6], in which most meteorological droughts identified using SPI12 were found to produce hydrological droughts.

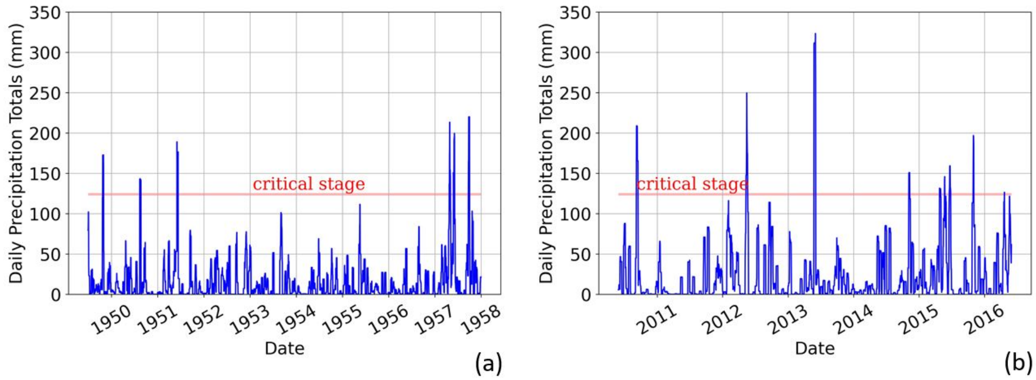

Figure 3: Daily precipitation totals at the San Antonio International Airport during two drought periods, including the period of 1949–1957 (a) and 2010–2015 (b). The critical stage is described by Eq. 2. Accordingly, PMet-drought in the San Antonio Pool ends after successive P_{RT} storms in 1957-1958 and in 2015, which enhanced the aquifer recharge. According to U.S. Geological Survey's estimates, the annual aquifer recharge in the Bexar county region increased from 2.47×10^6 m^3 in 1956 to 216.7 3×10^6 m^3 in 1957, and similarly, from 0.55×10^6 m^3 in 2014 to 162.3×10^6 m^3 in 2015.

Table 2: Necessary conditions for the occurrences of meteorological and groundwater droughts in the San Antonio Pool of the aquifer near the San Antonio International Airport.

Drought type	Condition	Minimum time period for the condition to persist
PMet-drought	$P_{RS-10d} < P_{RT}{}^*$	12 months
TMet-drought	$T_{RA-10d} > 32°C$	3 months
GW-drought	$GWL_{RA-10d} <$ CS stage-1†	3 months

* $P_{RT} = 123.95$ mm for the San Antonio Pool of the aquifer
† CS stage-1 = 201 m in accordance with the Critical Management Program implemented in the San Antonio Pool of the Edwards Aquifer Region

2.6. Explainable artificial intelligence (XAI) models

We used tree-based ensemble artificial intelligence models (AI), including Random Forest (RF) [62], eXtreme Gradient Boosting (XGBoost) [63], and Extremely Randomized Trees (ERT) [64] for AI-based supervised regression and classification modeling. The choice of these AI models is based on their high prediction accuracy and enhanced explainability of the results when they are coupled with post hoc explanatory methods [40, 54, 65–68]. In this study, we integrated these AI models with a post hoc explainability method called SHAP (discussed in Sec. 2.7) to extract valuable explanations from the underlying AI models.

We used AI regression models to predict time series of the intensity and duration of groundwater droughts as a function of lagged historical hydroclimatic features. In addition, after categorizing the groundwater drought intensity into a set of discrete classes (e.g., high-intensity or low-intensity droughts), we used AI classification models to predict the occurrences of groundwater drought classes using hydroclimatic and meteorologic drought features. In brief, the AI regression models allowed the prediction of time series of groundwater drought intensity while AI classification models unveiled the link between meteorological and groundwater droughts. AI-based regressors and classifiers can be generically expressed as:

$$\hat{y} = \phi(x) = \frac{1}{n} \sum_{k=1}^{n} f_k(x) \tag{3}$$

where $\hat{y}$ is the predicted outcome (continuous for regression and categorical for classification), $1 \leq k \leq n$, and f_1, f_2, ..., f_n are the functions learned by the n number of trees. Objective functions such as squared error, gini impurity, and logistic loss are used to learn the set of functions (f_k) by minimizing the difference between the predicted outcome ($\hat{y}$) and the actual outcome (y).

The GridSearch cross-validation technique in scikit-learn was used to tune the AI model's hyperparameters. It involves exhaustively searching over a specified hyperparameter space and evaluating the model performance using cross-validation. We used 3-fold cross-validation with a sample size of 75% from the train data set and the remaining for validation to ensure sufficient training data and a robust evaluation of the model. The set of hyperparameters with the lowest root mean square error (RMSE) was selected as the particular AI model hyperparameters and used to predict the test data. Two performance matrices, RMSE and coefficient of determination (R^2) were used to find the candidate AI model.

2.7. Post hoc explainability method - SHAP

As the direct interaction between the AI model features and target variable is not visible, sometimes it becomes difficult to interpret the AI models. SHAP is a post hoc explainability tool in the field of XAI, as XAI helps to create more transparent and interpretable models by providing insights into how different input variables influence the underlying models' prediction [37, 38]. SHAP uses Shapley values, a concept from cooperative game theory, to calculate the contribution of each player to the total payoff of a coalition. For the context of this study, Shapley values are used to quantify the contribution of each input variable to the predicted outcome. This approach considers all possible coalitions of input variables and calculates the expected contribution of each variable across all possible coalitions. By computing the Shapley values of each input variable, we can gain insights into how the model uses each variable to make predictions. We used AI regressors with SHAP to identify the most critical hydroclimatic features that influence the groundwater drought intensity. We used AI classifiers with SHAP to identify the relative importance of the duration and intensity of high temperature- or precipitation deficit-driven meteorological droughts on the intensity of groundwater droughts.

3. Results

In sections 3.1 - 3.4, we presented the duration, intensity, and frequency of historical meteorological and groundwater droughts in the San Antonio Pool of the aquifer computed using Eq. 1 with the baseline measures and prevailing conditions for droughts given in Table 2 and hydroclimatic data described in Section 2.3. Section 3.5.1 focused on the prediction of time series of historical groundwater drought intensity using AI regressors with hydroclimatic data and identification of the most influential hydroclimatic features in determining groundwater drought intensity. Section 3.5.2 dealt with predicting historical groundwater drought intensity classes based on hydroclimatic and meteorologic drought features using AI classifiers and uncovering the most critical meteorological drought features that drive groundwater drought intensity.

3.1. *High temperature-driven meteorologic droughts (TMet-droughts)*

The meteorological drought condition described in Table 2 by $T_{RA-10d} > 32°\mathrm{C}$ for at least 3 consecutive months identified 41 TMet-droughts in the region since 1940s, as shown in Fig. 4. The analysis revealed that the longest dry spell with $T_{RA-10d} \geq 32°\mathrm{C}$ took place in 2022, while longer extreme heatwaves with $T_{RA-10d} \geq 38°\mathrm{C}$ occurred four times more frequently after 2008 than for the period of 1946–2008. Moreover, although the duration of the TMet-droughts in the 1950s was longer than those during the 2010s drought, the intensity of TMet-droughts after 2008, in general, was higher than during the 1950s drought. By and large, TMet-droughts are well-aligned with GW-droughts in Fig. 4, although TMet-droughts occurred more often than GW-droughts. This is expected as TMet-droughts are less likely in the winter, and hence, could have a limited duration. A new TMet-drought could emerge as a result of seasonal changes in temperature while GW-drought can extend over seasons. Moreover, long extreme heatwaves with $T_{RA-10d} \geq 38°\mathrm{C}$ amplified the intensity of TMet-droughts.

3.2. *Precipitation deficit-driven meteorologic droughts (PMet-droughts)*

The meteorological drought condition described in Table 2 by $P_{RA-10d} <$ 123.95 mm for at least 12 consecutive months identified 25 PMet-droughts in the region since 1940s, as shown in Fig. 5. Although the most intense PMet-drought occurred in 2022, the PMet–drought condition lasted for 2,142 consecutive days during the 1950s, which marked the longest historical pre-

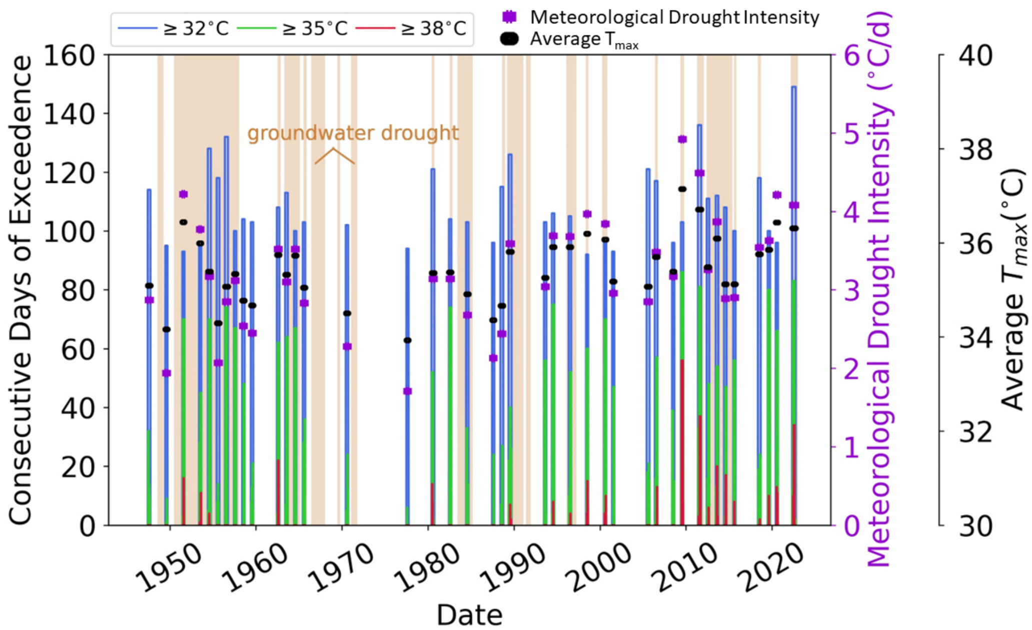

Figure 4: Historical TMet-droughts in the San Antonio Pool of the aquifer. Bars indicate the number of consecutive days with $T_{RA-10d} > 32$°C (blue+green+red), $T_{RA-10d} >$ 35°C (green+red), and T_{RA-10d} >38°C (red). The height of each bar corresponds to the duration of a TMet-drought event with T_{RA-10d} ≥32°C that occurs for at least 3 consecutive months. Average T_{max} is the average T_{RA-10d} over the drought duration. Drought intensity is computed using Eq. 1. GW-droughts, which will be discussed in the subsequent sections, are shown with light brown shading in the background as a reference.

cipitation deficit dry spell.

The second most-intense PMet-drought occurred from August 2007 through October 2009. Although short-term GW-droughts were associated with this PMet-drought, it may have had more of an impact on the intensity of the subsequent 2010s GW-drought, which was more intense than would be expected for the associated PMet-droughts during that period.

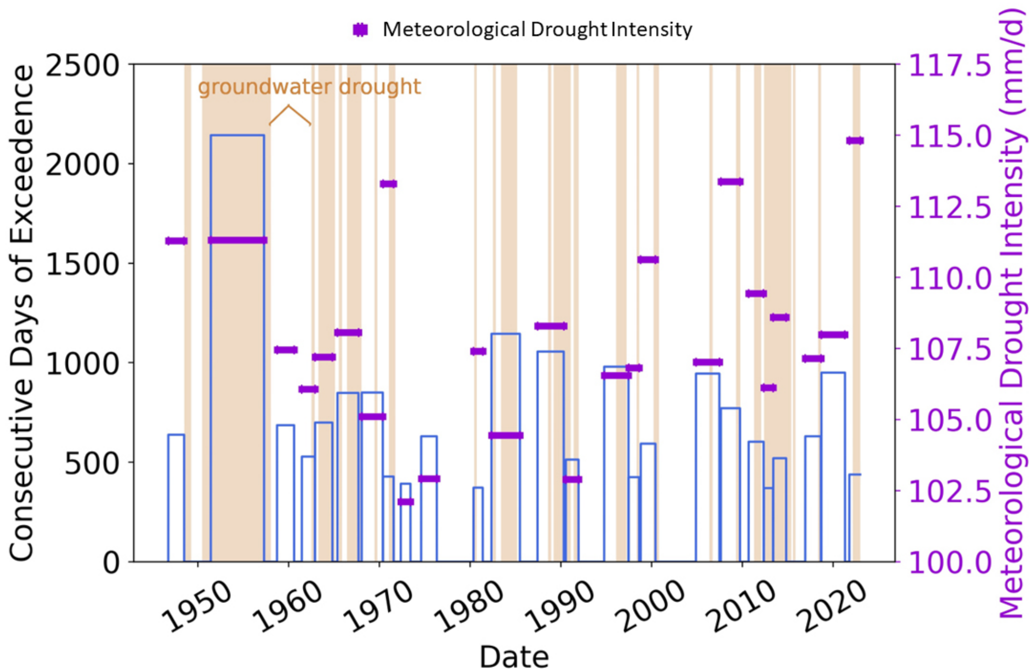

Figure 5: Precipitation deficit-driven historical meteorological droughts in the San Antonio Pool of the aquifer. The width of each bar denotes the start and end dates of drought and the height of a bar marks the drought duration with $P_{RS-10d} < 123.95$ mm that occurs for at least 12 consecutive months. Drought intensity is computed using Eq. 1. Groundwater droughts, which will be discussed in the subsequent sections, are shown with light brown shading in the background as a reference.

3.3. Low groundwater level-driven groundwater droughts (GW-droughts)

The groundwater drought condition described in Table 2 by $GWL_{RA-10d} <$ 201 m for at least 3 consecutive months identified 24 GW-drought events in the region since the 1930s, as shown in Fig. 6. The figure also shows the number of consecutive days GWL was below each CPM stage and reveals that as GWL fell below CPM-3 to CPM-5, GW-drought intensified more. In addition, the figure revealed three distinct historical GW-drought types that occurred in the 1950s, 2010s, and 2022.

The 1950s GW-drought was largely contributed by long and persistent precipitation deficiencies lacking succeeding P_{RT} storms until 1957, in conjunction with frequent high-intensity TMet-droughts. Although neither TMet- nor PMet-droughts were at their highest historical intensity in the 1950s, cumulative impacts of long duration and more frequent meteorological droughts resulted in the most-intense historical GW-drought. Hence, the longevity and persistency of meteorological droughts were more persuasive than their intensities on the GW-drought intensity in the 1950s.

Although meteorological droughts were not the longest or at the highest intensity during the 2010s drought, historically the highest intensity TMet-drought in June 2009 through September 2009 and the second highest intensity PMet-drought in August 2007 through October 2009 contributed to the third most intense GW-drought in the 2010s. High-intensity TMet-droughts and PMet-droughts in the preceding years likely lowered soil moisture and kept it unreplenished, which subsequently reduced the aquifer recharge and groundwater level recovery, and hence, increased the GW-drought intensity in the 2010s.

The 2022 GW-drought was driven by the longest dry spell with $T_{RA-10d} > 32°C$ and historically the most intense PMet-drought. Although the 2022 GW-drought lasted only for 12 months until January 2023, it emerged as the second most intense GW-drought on record. The top three most intense historical TMet-, PMet-, and GW-droughts in the San Antonio Pool of the aquifer on record are summarized in Table 3.

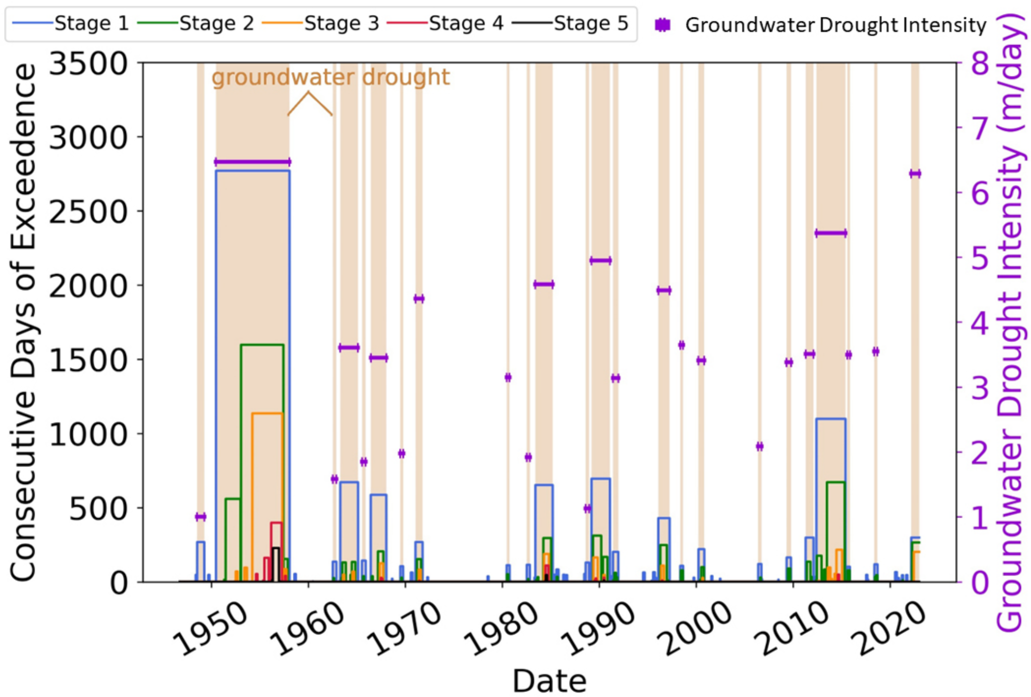

Figure 6: Low groundwater level-driven historical groundwater droughts in the San Antonio Pool of the aquifer. The width of each bar with a different color represents the start and end dates of a drought with different levels of severity and the height of each bar represents the drought duration $GWL_{RS-10d} < CPM_i$, where i corresponds to the five CPM stages in Table 1. Groundwater drought occurs when $GWL_{RS-10d} < CPM_1$ for 90 consecutive days. Drought intensity is computed using Eq. 1.

3.4. Intensity-duration-frequency analyses

Intensity-duration relationships of TMet-, PMet-, and GW-droughts are shown in Figs. 7a, c, e. In these plots, the most severe droughts with higher intensity and longer duration are found to the right and top of the figures. Fig. 7a shows that the San Antonio Pool experienced the most severe TMet-droughts with the longest duration in 2011 and 2022 since the 1950s drought of record. Similarly, since 2008, the region has experienced three out of four highest-intensity historical TMet-droughts in 2009, 2011, and 2020, which

Table 3: Top three most intense TMet-, PMet, and GW-droughts in the San Antonio Pool of the Edwards Aquifer Region.

Drought type	Start date	End date	Duration (d)	Intensity
PMet-drought	10/21/2021	12/31/2022	437	114.81 (mm/d)
	8/26/2007	10/3/2009	770	113.36 (mm/d)
	6/2/1970	8/2/1971	427	113.28 (mm/d)
TMet-drought	6/1/2009	9/11/2009	103	4.92 (°C/d)
	5/25/2011	10/7/2011	136	4.49 (°C/d)
	6/15/1951	9/15/1951	93	4.22 (°C/d)
GW-drought	6/27/1950	1/25/1958	2770	6.47 (m/d)
	9/3/2022	12/31/2022	298	6.29 (m/d)
	5/28/2012	5/30/2015	1098	5.37 (m/d)

were comparable or worse than the TMet-drought of 1951. These findings provide evidence for increasing stress due to elevated temperatures on the aquifer system over the past 15 years. Fig. 7c reveals that although the region experienced the longest PMet-droughts starting in 1951, it experienced intense PMet-droughts in 2007 and 2021 with a relatively shorter duration than the 1951s PMet-drought. Although the second longest PMet drought occurred in 1982 (998 days shorter than the 1950s drought), the highest intensity PMet-droughts occurred in 2007 and 2021.

Fig. 7e shows that historically the most severe GW-drought with the longest duration and highest intensity occurred starting in 1950. The second most severe GW-drought with the second longest duration occurred starting in May 2012. Although the recent GW-drought since March 2022 has a relatively short duration, it is the second most intense GW-drought on record and is driven by the historically most intense PMet-drought and the longest TMet-drought on record.

Although the TMet-drought intensity in the San Antonio Pool displayed a nearly bell-shaped distribution, PMet-drought and GW-drought intensity exhibited right-skewed distribution (Figs. 7b, d, f). Although high-intensity GW-droughts occurred less frequently historically (Figs. 7a-b), high-intensity meteorological droughts the San Antonio Pool embraced in recent years may alter the right-skewness of the frequency distribution of GW-drought in the future.

3.5. AI-based predictions of GW-droughts

We used tree-based ensemble AI regression and classification models, based on the RF, XGBoost, and ERT methods, to predict sporadic GW-droughts in the San Antonio Pool from hydroclimatic features. In the AI-based supervised regression modeling, a time series of GWL can be predicted from the current and lagged hydroclimatic and engineered AI features, as in [54]. The predicted GWL can then be used to calculate the intensity and duration of GW-droughts using Eq. 1 as part of post-processing. In the AI-based classification modeling, the appropriate number of GW-drought classes (e.g., intense vs. less-intense droughts) can be determined based on the uniformity of class sizes. The number of classes would be low if the size distribution of classes is highly uneven. The predictive accuracy of the AI-based model can then be evaluated based on true positives, false positives, true negatives, and false negatives in model predictions.

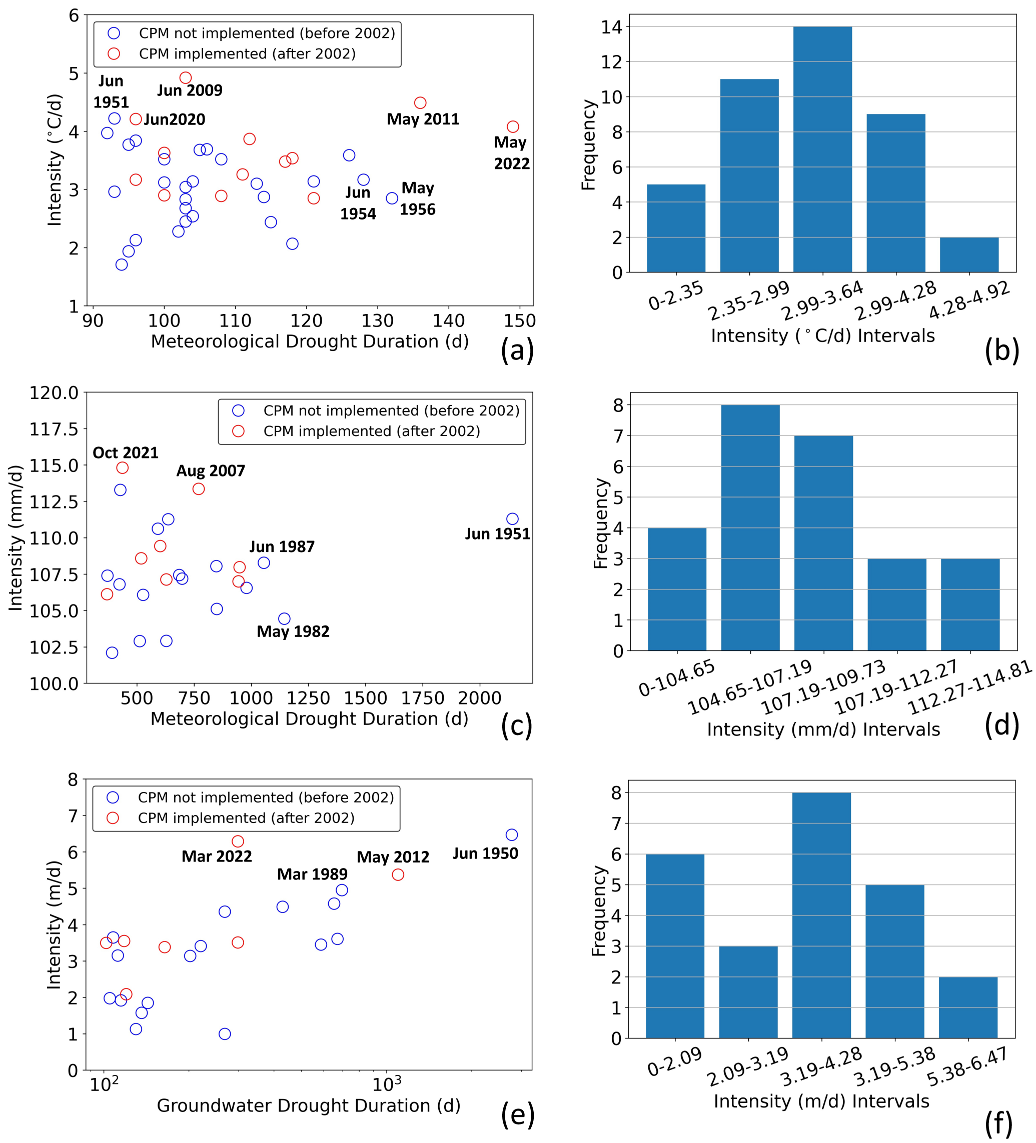

Figure 7: Intensity-duration relationships for high temperature-driven meteorologic droughts, precipitation deficit-driven meteorologic droughts, and low groundwater levels-driven groundwater droughts are shown in (a), (c), and (e) respectively. Their corresponding frequency of drought intensities are shown in (b), (d), and (f).

3.5.1. AI-based regression modeling

We initially used the month of the year, the current and the first three lags of P_{RS-10d}, T_{RA-10d}, and GWL_{RA-10d} as predictors to forecast GWL_{RA-10d}

on the next day sequentially. We used the 75% data from 11/1/1946 to 12/31/2010 to train the AI models and used the remaining 25% to test prediction accuracy of the models. Among these three AI models, ERT accomplished the best prediction accuracy (Table 4).

Table 4: Prediction accuracy of Random Forest (RF), Extremely Randomized Tree (ERT), and eXtreme Gradient Boosting (XGBoost) regressors, ERT with the reduced dimensionality (ERT-Red) using SHAP results, and the optimized ERT-Red (ERT-Red-OPT) through a 3-fold grid search cross validation technique on the randomly sampled training and testing data. Root mean square error (RMSE) and coefficient of determination (R^2) were used to assess the prediction performance of the models.

Predictand	AI Regressor	Data	RMSE(m)	R^2
GWL_{RA-10d}	RF	Training	0.107	1.0
		Testing	0.282	0.997
	XGBoost	Training	0.436	0.993
		Testing	0.452	0.992
	ERT	Training	0.0	1.0
		Testing	0.193	0.999
	ERT-Red	Training	0.0	1.0
		Testing	0.214	0.998
	ERT-Red-OPT*	Training	0.0	1.0
		Testing	0.211	0.998
		Validation	0.621	0.982

* The best subset of hyperparameters: Number of estimators = 139; Maximum depth of estimators = 41.

Next, we transformed the ERT model into an XAI model by coupling it with SHAP. The XAI model was used to identify the most critical features in the order of importance in predicting historical GWL_{RA-10d}, as shown in Fig. 8. In this figure, all the features below 'Month', including the past T_{RA-10d} and the second and third lags of P_{RS-10d} had insignificant impacts on GWL_{RA-10d} predictions; therefore, they were eliminated from further consideration. As a result, we set up a new ERT model with the reduced dimensionality (ERT-Red) that includes only the top 7 features in Fig. 8. To further improve the model predictivity, the ERT-Red model was optimized using a grid search algorithm. The optimization involved 200 candidates using a 3-fold grid search cross-validation technique, which equates to 600 model fits. The optimized model (ERT-Red-OPT) accomplished additional improvement on the ERT-Red model prediction accuracy on the test data (Table 4). Finally, we tested the predictive performance of the ERT-Red-OPT model on the validation data, including the same set of predictors and predictand, from 1/1/2011 to 1/1/2023, which was unseen by the ERT model during the training and testing phases. As reported in Table 4, the ERT-Red-OPT model accomplished high prediction precision on the validation data, and hence, emerged as a reliable predictor tool to forecast GWL_{RA-10d} from hydroclimatic features.

The predicted magnitude and trend of GWL_{RA-10d} in the validation data are statistically identical to the observed GWL_{RA-10d} (Table 4 and Fig. 9a). Slight differences in the predicted and observed GWL_{RA-10d} about the critical stage in June 2013 resulted in two separate back-to-back drought events for the period of 2012 to 2015 in AI-predicted results, shown in blue solid lines, in Fig. 9b. In fact, the combined duration of these two predicted GW-droughts is 1,095 days for the period of 2012-2015, which is only 3 days shorter than the observed GW-drought duration from the original data in Fig. 6 that corresponds to the top value of the red dashed line for the same period

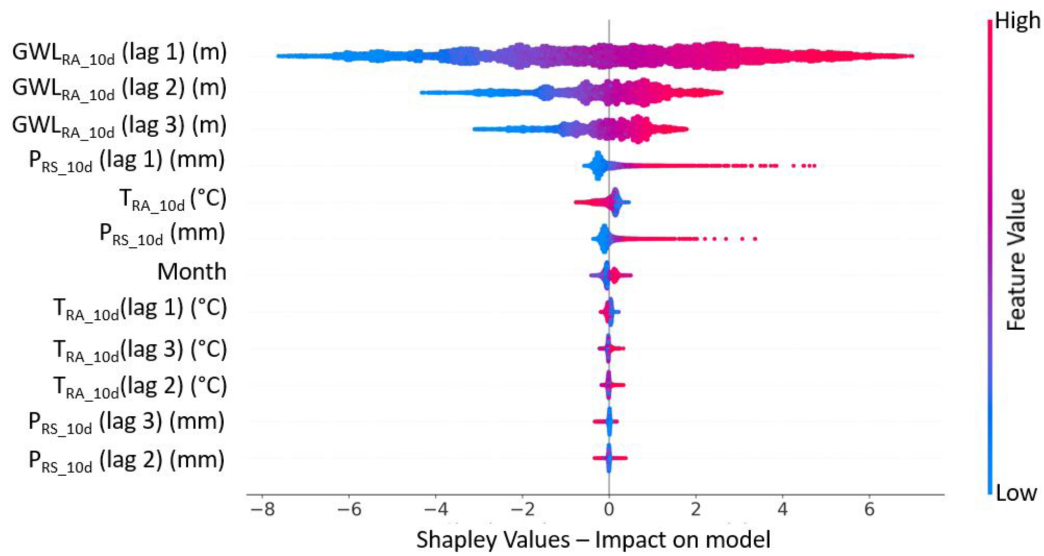

Figure 8: The order of importance of hydroclimatic features in predicting GWL_{RA-10d} using ERT coupled with the SHAP method. The most critical features are displayed at the top and the least critical features are displayed at the bottom. Hot and cold colors correspond to higher and lower feature values, respectively. For example, higher lagged GWL_{RA-10d}, and lagged and current P_{RS-10d} (represented by red dots) while lower T_{RA-10d} (represented by blue dots) are associated with higher GWL_{RA-10d} (represented by positive Shapley values on the x-axis), indicating that the results are consistent with expectations from underlying physics.

in Fig. 9. Similarly, the duration-weighted intensity of the AI-predicted two GW-droughts for the period of 2012-2015 is 5.19 m/d, which is only 3.3% lower than GW-drought intensity of 5.37 reported in Fig. 6. After all, ERT-Red-OPT emerged as a reliable predictive model to predict the time series of GW-droughts from hydroclimatic data. The main caveats of the method are: (i) GW-droughts are computed by post-processing AI-predicted GWL_{RA-10d}, and (ii) quantitative analysis in assessing the importance of the intensity and duration of TMet- and PMet-droughts on the intensity of GW-drought are not readily available from the associated SHAP analysis, which ranks the importance of hydroclimatic features in predicting GWL only. These two caveats have been addressed in the AI-based classification problem.

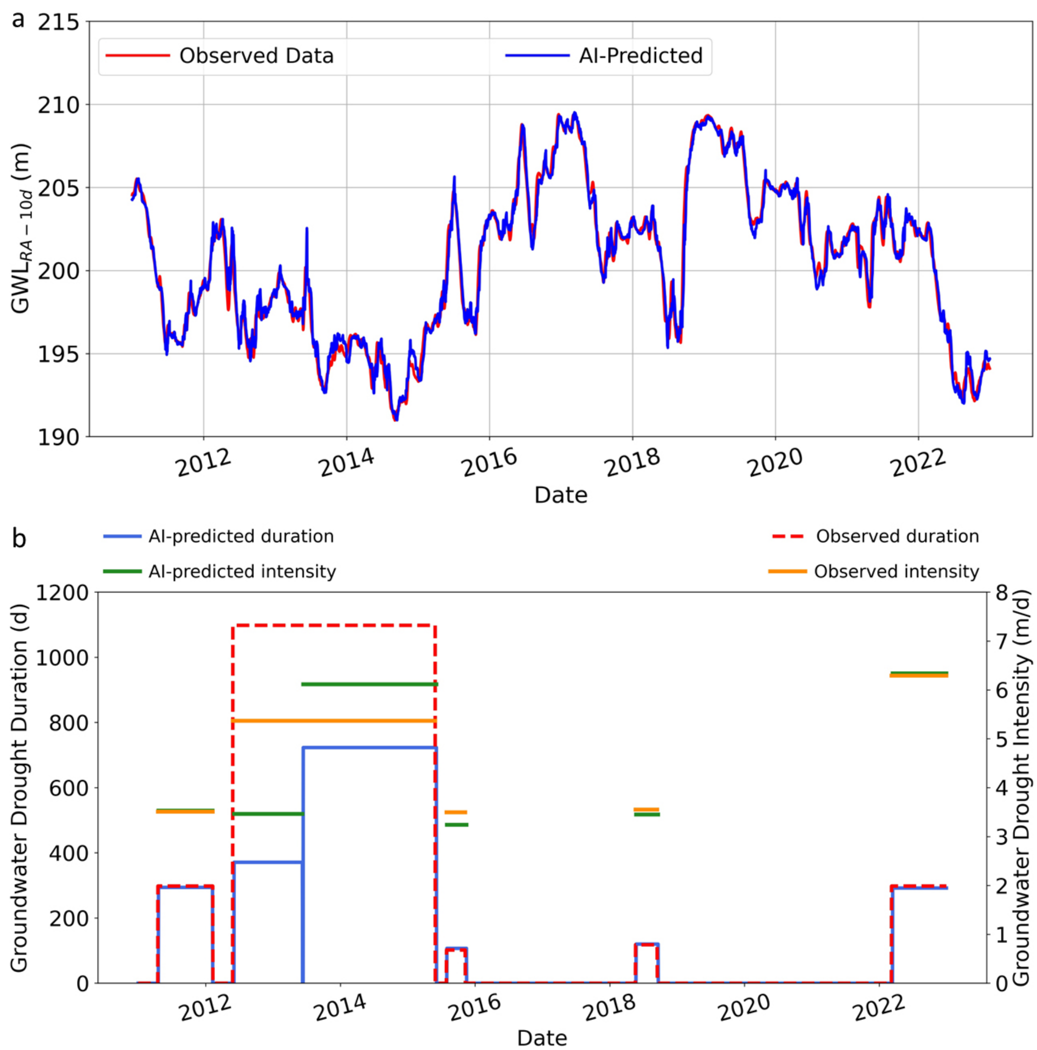

Figure 9: Original GWL_{RA-10d} in the validation data set and ERT-Red-OPT predicted GWL_{RA-10d} for the period of 1/1/2011 - 1/1/2023 using hydroclimatic features of the validation data set (a). Observed duration and intensity of GW-droughts (from Fig. 6) vs. AI (ERT-Red-OPT)-predicted duration and intensity of GW-droughts (b).

3.5.2. AI-based classification

The main purpose of the AI-based classification model is to unveil the relative importance of the intensity and duration of TMet- and PMET-droughts on the GW-drought intensity. We used RF, XGBoost, and ERT classifiers to predict the intensity of GW-drought from a set of climatic predictors, including the intensity and duration of PMet- and TMet-droughts, T_{RA-10d}, and P_{RS-10d}. Because the AI-based classifiers were set up for the discrete daily GWL-drought intensity, a proper number of class sizes needs to be determined based on the uniformity of sample size in each class. A histogram analysis in Fig. 10 shows that the class sizes became more unbalanced as the number of classes exceeded 2. Therefore, we focused on the formulation with 2 classes, in which GW-drought intensities in the range of 0-3.235 (Class-1) and 3.236-6.47 (Class-2) were labeled as 'mild GW-drought' and 'intense GW-drought', respectively. Because Class-2 is the minority class (whose sample size is about half of Class-1), we randomly oversampled (i.e., randomly duplicating samples) from the minority class and added them to the training and testing or only to the testing datasets. Through random oversampling, the originally imbalanced dataset was converted to a nearly balanced dataset, in which the numbers of days with intense drought or mild drought were made nearly equal. This step is crucial to avoid bias toward the majority class in model predictions. Using 75% of the data for training, ERT Classifier yielded the best predictive precision on the testing data (i.e., highest accuracy and F1-score) as shown in Table 5. According to the confusion matrix in Fig. 11a, daily 759 Class-1 events and 191 Class-2 events were accurately predicted by ERT. Although 39 daily Class-1 was inaccurately labeled as Class-2 and 107 daily Class-2 event were inaccurately labeled as Class-1, the overall prediction accuracy of 86.09% (F1-score) for discrete GW-drought is deemed to be very good. Next, the ERT Classifier was transformed into an XAI model by interfacing it with SHAP, and the corresponding global SHAP analysis results are shown in Fig. 11b. According to these results, the duration of PMet-drought and intensity of TMet-drought are the topmost critical meteorological drought features in order of importance in predicting GW-drought intensity. The global SHAP analysis also reveals that elevated temperature is pivotal for more intense GW-droughts in the San Antonio Pool of the aquifer, suggesting that precipitation deficits would result in more intense GW-droughts when temperatures are high.

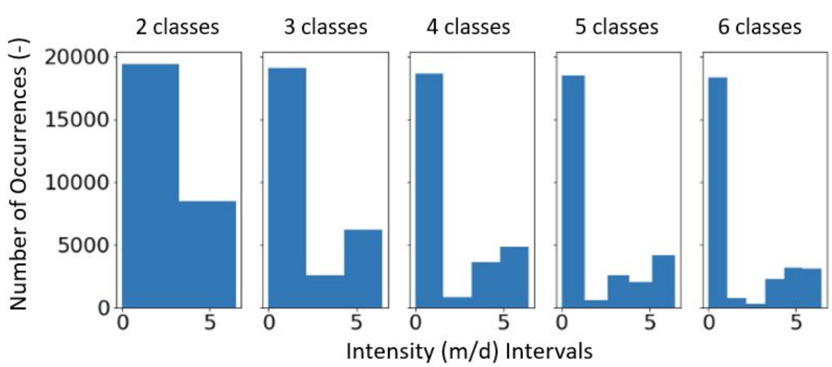

Figure 10: Number distributions of daily GW-drought intensity in each GW-drought class. Uniform bin sizes were used in each plot in the range of 0-6.47 m/d. For example, the class sizes were 0 - 3.235 m/d and 3.235 - 6.47 in the left-most plot. The distribution of GW-droughts becomes more unbalanced as the number of classes exceeds 2.

Table 5: Prediction accuracy measures of the RF, Extremely Randomized Tree (ERT), and eXtreme Gradient Boosting (XGBoost) classifiers on the randomly oversampled training and testing data or on the testing data.

Predictand	AI Classifier	Data	Accuracy(%)	Precision(%)	Recall(%)	F1-score(%)
Intensity	RF	ROTT*	94.46	94.47	94.46	94.46
		Testing	86.04	85.64	86.04	85.54
	XGBoost	ROTT	85.16	85.46	85.16	85.13
		Testing	77.10	76.84	77.10	76.96
	ERT	ROTT	95.0	95.0	95.0	95.0
		Testing	86.68	86.39	86.68	86.09

* ROTT: Randomly oversampled training and testing data.

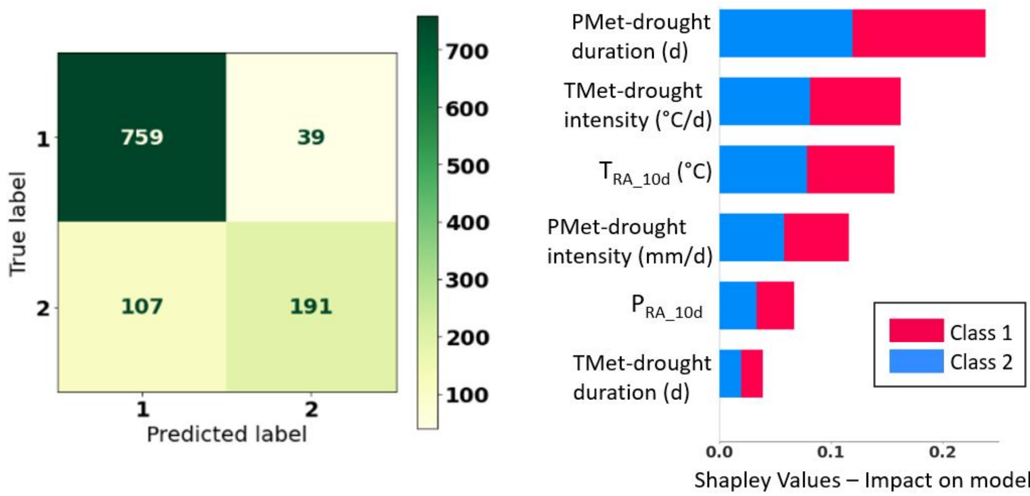

Figure 11: The confusion matrix for the test data using the ERT-Classifer (a) and the order of importance of the features in predicting the GWL-drought intensity computed by the Global SHAP analysis (b). The most critical features in predicting the intensity of GW-droughts are shown at the top in (b).

4. Discussion

4.1. Baseline measures and conditions for TMet-, PMet-, and GW- droughts

We established novel baseline measures and prevailing drought conditions for TMet, PMet, GW-droughts based on region-specific hydroclimatic data.

Because sustained precipitation deficits [41] or high temperature and evapotranspiration [42] could be the main driver for droughts, we computed the duration, intensity, and frequency of high TMet- and PMet-droughts separately - different from the earlier GW-drought assessment models - but analyzed their combined impacts on the intensity-duration of GW-droughts. Although we used the general description of heatwaves by the National Weather Service in defining the dry spell and condition for TMet droughts, we used region-specific data associated with successive severe storms and enforced mitigation measures in the region in establishing the baseline measures and prevailing conditions for PMet-droughts and GW-droughts, respectively. We demonstrated that high precipitation deficits alone, as implemented by [55], are not representative of PMet-droughts in the San Antonio Pool of the karstic aquifer, where succeeding severe storms, associated with the focused recharge, are the main mechanism to alleviate GW-droughts. To our knowledge, enforced mitigation measures have been used in this study for the first time to identify and characterize groundwater droughts.

4.2. Link between TMet- and PMet-droughts and GW-droughts

Separate calculation of the duration, intensity, and frequency of TMet-droughts and PMet-droughts is the novel approach in our drought risk assessments. Our analysis revealed that the interplay and competition between TMet-drought and PMet-drought could suppress or effectively lower the GW-drought intensity. For example, the effects of high-intensity TMet-drought in 1958-1959 and 1977 on GW-drought were offset by low-intensity PMet-drought. Like the 1950s GW-drought, the 2010s GW-drought intensified by heatwave strikes ended by succeeding heavy storms in 2015. Interestingly, high-intensity TMet-droughts and relatively high-intensity PMet-droughts in 2020 did not result in intense GW-droughts. These events likely contributed to the intensity of the 2022 GW-drought but were likely mitigated by timely heavy storms (P_{RT}) in early 2021. Consistent with our finding, combined effects of temperature and precipitation on droughts are evident from the earlier analyses, in which precipitation deficits in California, for example, were found to be more than twice as likely to result in drought years if they occur in warm conditions [69].

Fig. 7e demonstrates that GW-drought intensity in general increases with drought duration, in agreement with the findings in [70]. The same conclusion, however, is not applicable for TMet- and PMet-droughts (Fig. 7a-e), as the memory effect is critical for GW-drought rather than for meteorological droughts. Ref. [17] reported a longer mean duration for GW-drought in unconsolidated aquifers than for PMet-droughts in Jiangsu Province of China. We observed the opposite in our study area, in which the mean duration of PMet-drought and GW-drought is 724 days and 407 days, respectively, revealing that the deeper karstic Edwards aquifer system is more resilient to precipitation deficits.

The arithmetic/geometric means of the duration of GW-, PMet- and TMet- droughts were 406/253, 694/626, and 108/107 days. After comparing the cumulative distribution functions of PMet- and GW-droughts obtained from numerical experiments with a simple water balance model and real climate data from multiple locations across the globe, [6] articulated that shorter GWL-drought than PMet-drought could be associated with larger rainfall amounts than evaporation losses, which could result in sustainable aquifer recharge and shorter GW-droughts even in the periods of low rainfall. This postulation is, however, not applicable to the semi-arid karstic San Antonio Pool of the aquifer, as the extreme precipitation events and the resultant large focused recharge would be needed to end GW-drought in the region (Fig. B.2), where evapotranspiration losses frequently exceed rainfall most of the year.

4.3. Regional GW-drought types

Our analyses identified three distinct historical GW-droughts - with the newly introduced terminologies reflecting the nature of the link between meteorological and groundwater droughts - in the San Antonio Pool of the aquifer. The 1950s GW-drought is a 'persistence-driven drought', driven by the persistency of a series of medium to high-intensity meteorological droughts over seven consecutive years lacking severe storms. 2010 GW-drought is, however, a 'preconditions-driven drought', driven by high-intensity meteorological droughts in the preceding months or years that could have effectively reduced antecedent soil moisture, aquifer recharge, groundwater level recovery [71–73]. The 2022 GW-drought is an intensity-driven drought, driven by the longest high temperature-driven dry spell and historically the most intense PMet-drought. Unlike the 1950s GW-drought, GW-droughts in 2010s and 2022 occurred when aquifer protection strategies were in effect. Thus, the intensity of the 2010s and 2022 GW-droughts could have been greater without these strategies. However, quantitative assessment of regional mitigation impacts on GW-droughts is beyond the scope of this paper.

4.4. Predictability of GW-drought intensity

We introduced novel explainable AI models for higher predictability of targeted variables and enhanced explainability of AI-based predictions. Our AI-based analyses revealed that tree-based ensemble AI models are effective in predicting GW-drought intensity using regional hydroclimatic data. Among the hydroclimatic features, the first three lags of the groundwater levels, current temperature, and current precipitation were found to be the most influential features in the order of importance for groundwater drought intensity predictions. Relatively higher importance for temperature than precipitation suggests that precipitation deficits would lead to more intense GW-droughts when temperatures are high, which agrees with the findings in [69]. The AI-based analyses further unveiled that the duration of the PMet-drought and the intensity of the TMet-drought are the most critical features in the order of importance for more accurate prediction of GW-drought intensity from meteorological drought features. Such new knowledge was discoverable only because our novel drought identification approach allowed the characterization of TMet- and PMet-droughts separately.

4.5. Evidence of climate change from the drought assessment

Using the new drought identification scheme, the analysis identified the longest high-intensity TMet-droughts in 2011 and 2022, the longest dry spell on record in 2022, and the longest heatwaves after the year 2008. In addition, although the region experienced the most severe PMet-drought with the longest duration in the 1950s, it experienced historically the highest intensity PMet-drought in 2007 and 2021. These findings provided compelling evidence that the climate in the region has been warming over the past 15 years.

4.6. Limitations - suitability of our approach for data-scarce regions

Although our data-driven drought characterization and prediction schemes are highly encouraging, they require long-term and trustable hydroclimatic data to produce reliable results. In addition, regional mitigation measures are needed to establish baseline measures and conditions for GW-droughts. Although we have such data available for the San Antonio Pool of the aquifer since the 1940s, this may not be the case in many other regions, and hence, may limit the application of our drought identification scheme to other regions. However, it is possible to overcome this limitation with remote sensing datasets and numerically generated synthetic data. Moreover, baseline measures can be constrained better when the drought identification scheme is applied to more regions with different hydroclimatic characteristics.

4.7. Future work - prediction tool for future GW-drought intensity predictions

Because projected time-series of daily temperature and precipitation for the San Antonio Pool of the aquifer from 2023 to 2100 under different climate scenarios can be downscaled from global climate models [54], and the projected temperature and precipitation can then be used to calculate projected PMet- and TMet-droughts in the future using our drought identification scheme, the explainable AI models described in this paper can then be used to project GW-droughts from 2023 through 2100. This will be addressed in future work.

5. Conclusions

We presented a new drought characterization scheme to determine the intensity, duration, and frequency of high temperature- and precipitation deficit-driven meteorological droughts and low groundwater level-driven groundwater droughts in a semi-arid karstic region. We also demonstrated the use of explainable AI models for reliable time series prediction of groundwater drought intensity from hydroclimatic variables and the identification of the most influential meteorological drought features on GW-drought intensity. The main conclusions are as follows:

1. Newly-defined three distinct historical groundwater drought types, including persistence-driven, preconditions-driven, and intensity-driven

GW-drought were identified in the semi-arid karstic region.

2. Dynamic interactions between PMet- TMet-droughts were found to determine the duration and intensity of GW-droughts. In some cases, they canceled each other's impacts on groundwater drought.

3. The new drought intensity identification scheme provided compelling evidence for a warming climate, consequently, intensifying hydrologic cycle and increasing stress on the regional aquifer over the past 15 years.

4. The new explainable AI model predicted time series of groundwater drought intensity with high precision using historical hydroclimatic features. The first three lags of the groundwater level data along with the current temperature and precipitation data were found to be the most decisive features in the order of importance in predicting groundwater drought intensity.

5. The new explainable AI model disclosed that the duration of the precipitation deficit-driven meteorological drought and the intensity of the high temperature-driven meteorological drought were found to be the most influential features in the order of importance in predicting groundwater drought intensity.

6. AI-based predictive models consistently assigned higher importance to high temperature than precipitation deficits in predicting groundwater drought intensity, suggesting that the impacts of precipitation deficit-driven groundwater droughts in the region would be more intense at

elevated temperatures.

The new drought identification scheme and the explainable AI models can potentially serve as a reliable predictive tool to forecast the intensity, duration, and frequency of future groundwater droughts using scenario-based projected climate data from global climate models.

CRediT authorship contribution statement

Hakan Başağaoğlu: Conceptualization; Formal analysis; Investigation; Methodology; Software; Visualization; Writing - original draft, review & editing. **Chetan Sharma**: Conceptualization; Formal analysis; Investigation; Methodology; Software; Writing -review & editing. **Debaditya Chakraborty**: Conceptualization; Formal analysis; Investigation; Methodology; Software; Visualization; Writing - original draft, review & editing. **Icen Yoosefdoost**: Formal analysis; Investigation; Writing -review & editing. **F. Paul Bertetti**: Conceptualization; Project administration; Resources; Supervision; Writing - review & editing.

Declaration of Competing Interest

The authors declare that they have no known competing financial interests or personal relationships that could have appeared to influence the work reported in this paper.

Acknowledgements

This research was supported by the Edwards Aquifer Authority (Project # SAT0003616). Any opinions, findings, conclusions, or recommendations expressed in this publication are solely those of the authors. The authors thank Chad Furl of EAA for his comments on the initial version of the manuscript, Logan Schmidt of EAA for his confirmatory analyses on groundwater droughts, and Bryan Anderson and Newfel Mazari of EAA for data collection. The authors also thank Sarah Eason of EAA for her help with the preparation of the location map.

Abbreviations

Commonly used abbreviations in the paper:

AI	Artificial Intelligence
CPM	Critical Period Management
D	Drought Duration
EAA	Edwards Aquifer Authority
EAR	Edwards Aquifer Region
ERT	Extremely Randomized Trees
GW-drought	Groundwater drought

GWL_{RA-10d} ... 10-day rolling-averaged daily groundwater levels

P .... Precipitation

PMet-drought . Precipitation deficit-driven meteorologic drought

P_{LT} .... Left tail of precipitation distribution

P_{RT} .... Right tail of precipitation distribution

P_{RS-10d} .... 10-day rolling-summed daily precipitation totals

RF .... Random Forest

RMSE .... Root Mean Square Error

R^2 .... Coefficient of determination

SHAP .... SHapley Additive exPlanations

TMet-drought . High temperature-driven meteorologic drought

T_{max} .... Maximum air temperature

T_{min} .... Minimum air temperature

T_{RA-10d} .... 10-day rolling-averaged daily maximum temperatures

XAI .... eXplainable Artificial Intelligence

XGBoost ...... Extreme Gradient Boosting

Appendix A. Suitability of Groundwater Level Data at the J-17 Index Well and Climate Data at the San Antonio International Airport (SAT) for the Drought Assessment in the San Antonio Pool of the Aquifer

In this section, we provide technical justification for the representativeness of groundwater levels from the J-17 index well and climate data from the SAT for the hydroclimatic conditions for the San Antonio pool of the Edwards aquifer system.

Appendix A.1. Representativeness of groundwater levels from the J-17 index well for the San Antonio Pool of the Edwards Aquifer

Flow within the aquifer is from higher to lower elevations and generally west to east, where the aquifer has major natural discharge points at the Comal and San Marcos springs systems. Flow magnitude and direction are significantly impacted by faulting, and a series of structural features in the Artesian Zone in the western portion of the aquifer form a hydraulic restriction to flow from west to east in that area. This restriction is known locally as the Knippa Gap and is located in the subsurface approximately along the reach of the Frio River within the Uvalde County Artesian Zone. The hydraulic behavior of the aquifer is different across this restriction—the Uvalde Pool in the west has semi-confined characteristics while the San Antonio Pool to the east is primarily a confined system, and the pools are managed separately to account for this difference.

To make regulatory management clearer, the San Antonio Pool extent is arbitrarily defined at the boundary between Uvalde and Medina counties even though the physical barrier is a few kilometers to the west of the boundary. The San Antonio Pool accounts for about two-thirds of the areal extent of the aquifer. The confined, artesian nature of the San Antonio Pool produces similar pressure change responses to recharge and discharge events across the Pool. Within the Artesian Zone of the San Antonio Pool, dissolution, fractures, and conduits have resulted in significant permeability throughout the Edwards Group limestones so that wells are very productive in the freshwater portion of the aquifer irrespective of location (e.g., [36, 52, 74]). This consistency in hydraulic behavior has been recognized since the 1930s, and a single well with an extensive record of water level data (known as J-17) has been designated as the index well for the San Antonio Pool. Water level data from the index well and two other wells in the western and eastern areas of the San Antonio Pool are shown in Fig. A.1 below. The response of the system is similar in all three wells and the water levels are highly correlated, with the differences in head due to the west-to-east hydraulic gradient. Thus, J-17 is an adequate representation of the hydraulic conditions of the San Antonio Pool despite its large areal extent.

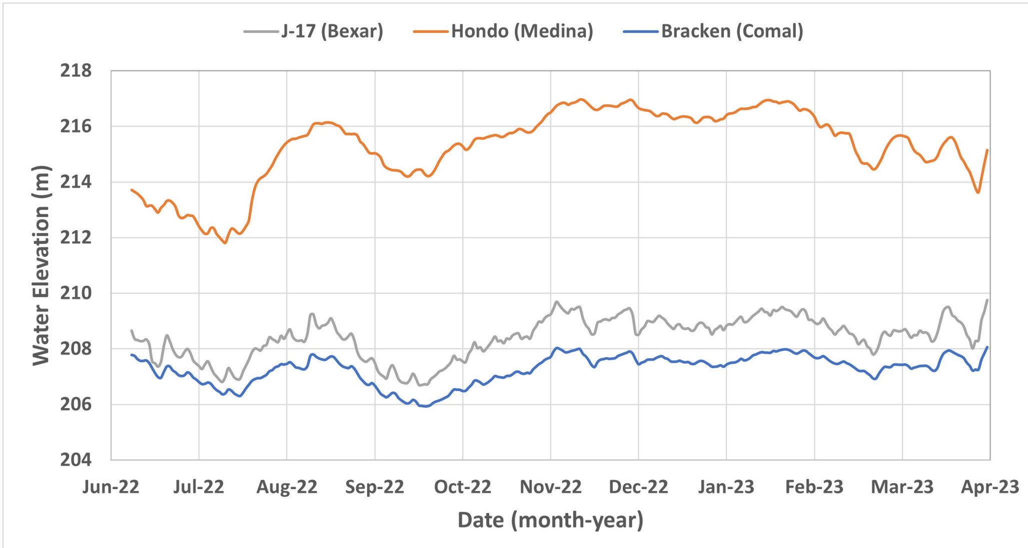

Figure A.1: Temporal changes in groundwater levels at the J-17, Hondo (Medina), and Bracken (Comal) well within the San Antonio Pool of the Edwards Aquifer Region. The location of these wells is shown in Fig. A.2.

Appendix A.2. Representativeness of the climate data at the SAT for the San Antonio Pool of the Edwards Aquifer

Next, we address the *representativeness of the climate data from the SAT for the San Antonio Pool of the aquifer systems.* While the variability in temperature and precipitation adds more uncertainty to the use of a single weather station, there are few high-quality long-term weather records in the region associated with the San Antonio Pool, and the SAT location has a high-quality long-term record. Nonetheless, the SAT location adequately represents the system for the purposes of evaluating the drought model beyond the length of the record. Mean temperature and annual precipitation in the region are influenced significantly by the topographic changes associated with the Balcones Fault Zone. 30-yr normals for mean temperature and annual precipitation [75, 76] are shown in Figs. A.2 and A.3 below.

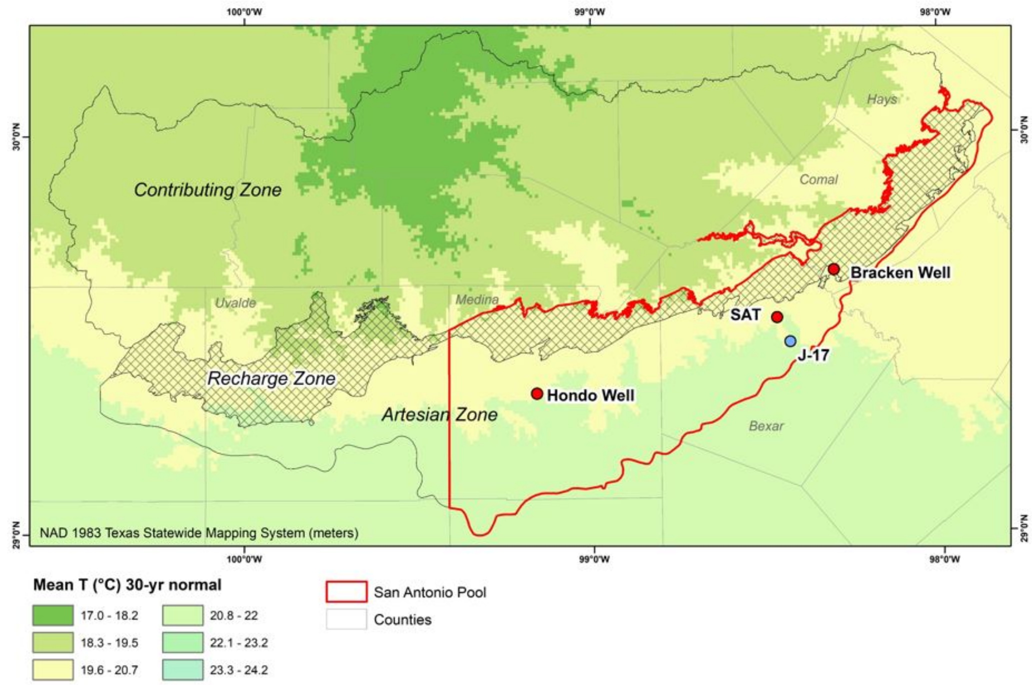

Figure A.2: 30-year normal annual temperatures across the Edwards Aquifer region.

As shown in Fig. A.2, the SAT location is quite representative of regional variability with respect to mean temperatures in the Recharge Zone of the San Antonio Pool. There is a maximum of a 1°C variation in mean temperature across the Recharge Zone for the San Antonio Pool. While daily temperatures may vary more so, over the time frame of interest to the drought calculations (months, typically), use of SAT data is representative.

The distribution of annual average precipitation for the Edwards Aquifer Region shows more variability across the Recharge Zone of the San Antonio

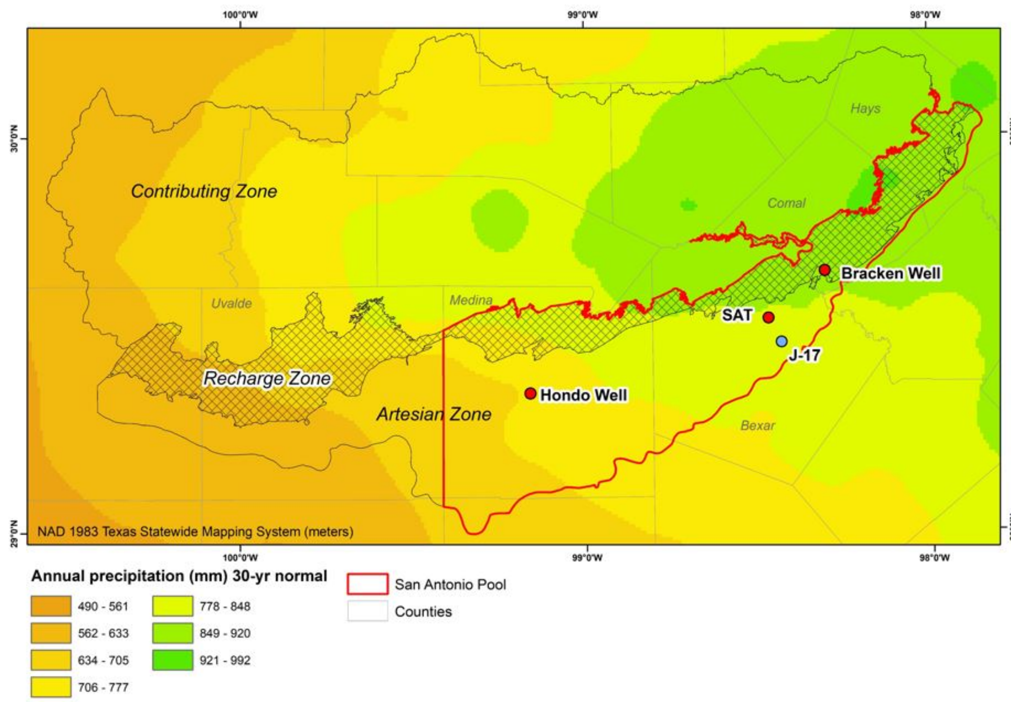

Figure A.3: 30-year normal annual precipitation across the Edwards Aquifer Region.

Pool (Fig. A.3). There is a notable extension of precipitation contours from east to west that is caused by the topographic changes associated with the Balcones Fault Zone. This "tongue" has the effect of making annual precipitation in the western part of the Recharge Zone of the San Antonio Pool more like that of the SAT location than would be expected (precipitation changes significantly east to west in other areas of Texas, especially near the 100th W meridian). Annual precipitation values range from a maximum of about 920 mm in the east to about 760 mm in the west. The annual average value at the SAT is 841 mm, which is suitably centered in the range of precipitation values. Importantly, most recharge for the San Antonio Pool is derived from outcrops near and to the west of SAT rather than from the Recharge Zone exposed in the northeast (e.g., [36]). Thus, the actual precipitation range of interest is more like 760 to 860 mm, which makes the SAT data even more suitable.

It should be also noted that the recharge within the San Antonio Pool effectively increases pressure throughout the pool because of its interconnected and highly confined nature. Therefore, while spatial variability can be important for specific events, the similarities in 30-yr normals for temperature and precipitation between the SAT location and the region of interest for recharge in the San Antonio Pool allow for effective use of SAT data even if it is a single-point dataset.

Appendix B. Precipitation Deficiencies-driven Meteorological Droughts Based on the 15$^{\mathrm{th}}$-Percentile Criteria

In recent precipitation deficiency-driven meteorological drought analyses, months with 3-month rolling-averaged P totals (P_{RA-3m}) below the 15$^{\mathrm{th}}$ percentile of the P_{RA-3m} were considered to be drought [55]. When we applied this meteorological drought definition to the 1950s and 2010s droughts in the EAR, it failed to accurately capture meteorological droughts associated with the observed groundwater droughts, as most of the dry months were inaccurately identified as non-drought (Fig. B.1).

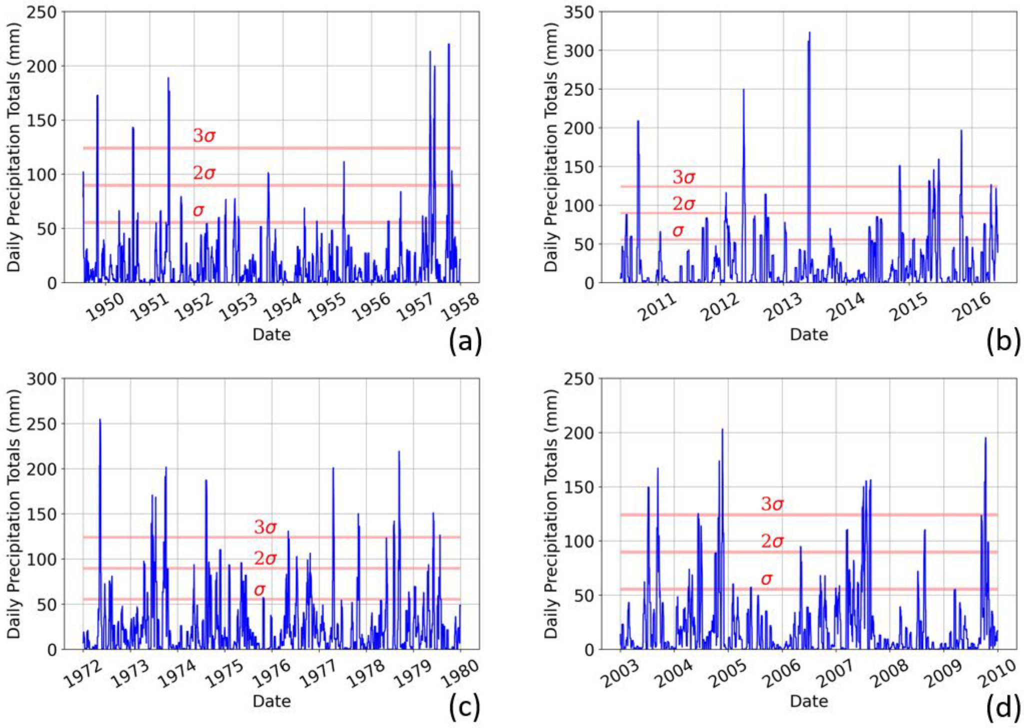

Figure B.1: Monthly precipitation totals at the SAT (located in the San Antonio Pool of the semi-arid Edwards Aquifer Region) during two severe groundwater drought events that occurred in the period of 1949-1957 (a) and 2010-2012 (b). The critical stage in these plots refers to the 15^{th} percentile of the 3-month rolling-averaged monthly precipitation totals (P_{RA-3m}), as suggested by [55]. Accordingly, months with P_{RA-3m} below the critical stage are considered to be in drought. Clearly, this measure does not accurately represent meteorological droughts driven by precipitation deficiencies in the region.

References

[1] A. F. Van Loon, Hydrological drought explained, WIREs Water 2 (2015) 359–392. doi:10.1002/wat2.1085.

[2] A. K. Mishra, V. P. Singh, A review of drought concepts, Journal of Hydrology 391 (2010) 202–216. doi:10.1016/j.jhydrol.2010.07.012.

[3] J. R. Heim, A review of twentieth-century drought indices used in

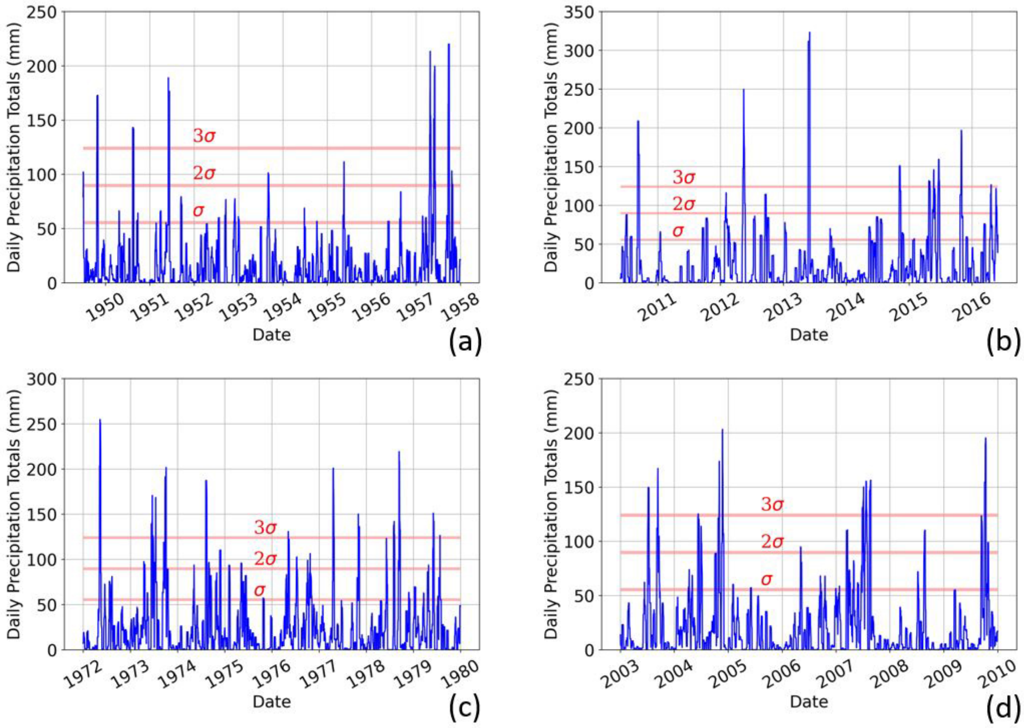

Figure B.2: n in Eq. 2 is used to account for the influence of the right tail of precipitation totals (P_{RT}) on groundwater droughts. Each red line corresponds to $\mathrm{P}_{\mu,RS-10d}$ + $\mathrm{P}_{SD,RS-10d}$, where the standard deviation, SD = σ, 2σ, or 3σ. n = 3 reasonably well-represented meteorological droughts associated with persistent severe groundwater droughts in the 1950s (a) and 2010s (b). Successive P_{RT}s in 1957-58 and 2015 ended the 1950s and 2010s GW-droughts, respectively. n = 3 also reasonably well represented the periods with less intense to nonexistent GW-droughts in the 1970s (c) and 2000s (d). The duration and intensity of historical groundwater droughts are shown in Fig. 6.

the United States, Bull. Am. Meteorol. Soc 83 (2002) 1149–1166. doi:10.1175/1520-0477-83.8.1149.

[4] S. D. Crausbay, A. R. Ramirez, S. L. Carter, M. S. Cross, K. R. Hall, D. J. Bathke, J. L. Betancourt, S. Colt, A. E. Cravens, M. S. Dalton, Defining ecological drought for the twenty-first century, Bull. Amer. Meteor. Soc. 98 (2017) 2543–2550. doi:10.1175/BAMS-D-16-0292.1.

[5] E. A. B. Eltahir, P. J.-F. Yeh, On the asymmetric response of aquifer water level to floods and droughts in Illinois, Water Resources Research 35 (1999) 1199–1217. doi:10.1029/1998WR900071.

[6] T. Apurv, M. Sivapalan, X. Cai, Understanding the role of climate characteristics in drought propagation, Water Resources Research 53 (2017) 9304–9329. doi:10.1002/2017WR021445.

[7] A. Pathak, B. Dodamani, Trend analysis of groundwater levels and assessment of regional groundwater drought: Ghataprabha river basin, India, Nat. Resour. Res. 282 (2019) 631–643. doi:10.1007/s11053-018-9417-0.

[8] H. A. J. Van Lanen, E. Peters, Definition, Effects and Assessment of Groundwater Droughts, Springer Netherlands, Dordrecht, 2000, pp. 49–61.

[9] B. Kløve, P. Ala-Aho, G. Bertrand, J. J. Gurdak, H. Kupfersberger, J. Kværner, T. Muotka, H. Mykrä, E. Preda, P. Rossi, C. B. Uvo, E. Velasco, M. Pulido-Velazquez, Climate change impacts on groundwater and dependent ecosystems, Journal of Hydrology 518 (2014) 250–266. doi:10.1016/j.jhydrol.2013.06.037.

[10] R. Ghasemizadeh, F. Hellweger, C. Butscher, I. Padilla, D. Vesper, M. Field, A. Alshawabkeh, Review: Groundwater flow and transport modeling of karst aquifers, with particular reference to the North Coast

Limestone aquifer system of Puerto Rico., Hydrogeol J. 20 (2012) 1441–1461. doi:10.1007/s10040-012-0897-4.

[11] R. Ghasemizadeh, X. Yu, C. Butscher, F. Hellweger, I. Padilla, A. Alshawabkeh, Equivalent porous media (epm) simulation of groundwater hydraulics and contaminant transport in karst aquifers, PloS One 10 (2015) e0138954. doi:10.1371/journal.pone.0138954.

[12] H.-R. Byun, D. Wilhite, Objective quantification of drought severity and duration, Journal of Climate 12 (1999) 2747–2756. doi:10.1175/1520-0442(1999)012<2747:OQODSA>2.0.CO;2.

[13] T. McKee, N. Doesken, J. Kleist, The relation of drought frequency and duration to time scales. 8th Conference on Applied Climatology, Anaheim, California, 17-22 January, 1993, pp. 179–184.

[14] S. M. Vicente-Serrano, S. Beguería, J. I. López-Moreno, A multiscalar drought index sensitive to global warming: The standardized precipitation evapotranspiration index, Journal of Climate 23 (2010) 1696–1718. doi:10.1175/2009JCLI2909.1.

[15] I. Nalbantis, G. Tsakiris, Assessment of hydrological drought revisited, Water Resources Management 23 (2009) 881–897. doi:10.1007/s11269-008-9305-1.

[16] J. P. Bloomfield, B. P. Marchant, Analysis of groundwater drought

building on the standardised precipitation index approach, Hydrol. Earth Syst. Sci. 17 (2013) 4769–4787. doi:10.5194/hess-17-4769-2013.

[17] X. Liu, B.and Zhou, W. Li, C. Lu, L. Shu, Spatiotemporal characteristics of groundwater drought and its response to meteorological drought in Jiangsu province, China, Water 8 (2016) 480. doi:10.3390/w8110480.

[18] S. Sadeghfam, R. Mirahmadi, R. Khatibi, A. Nadiri, Investigating meteorological/groundwater droughts by copula to study anthropogenic impacts, Sci Rep 12 (2022) e2020GL087820. doi:10.1038/s41598-022-11768-70.

[19] Z. Wu, H. Xu, Y. Li, L. Wen, J. Li, G. Lu, X. Li, Climate and drought risk regionalisation in China based on probabilistic aridity and drought index, Science of The Total Environment 612 (2018) 513–521. doi:10.1016/j.scitotenv.2017.08.078.

[20] M. D. Svoboda, B. A. Fuchs, C. C. Poulsen, J. R. Nothwehr, The drought risk atlas: Enhancing decision support for drought risk management in the United States, Journal of Hydrology 526 (2015) 274–286. doi:10.1016/j.jhydrol.2015.01.006.

[21] O. Rahmati, F. Falah, K. S. Dayal, R. C. Deoe, F. Mohammadi, T. Biggs, D. D. Moghaddam, S. A. Naghibi, D. T. Bui, Machine learning approaches for spatial modeling of agricultural droughts in the south-

east region of Queensland Australia., Sci. Total Environ. 699 (2020) 134230. doi:10.1016/j.scitotenv.2019.134230.

[22] C. Sharma, C. S. P. Ojha, Changes of annual precipitation and probability distributions for different climate types of the world, Water 11 (2019) 2092. doi:10.3390/w11102092.

[23] J. Laimighofer, G. Laaha, How standard are standardized drought indices? Uncertainty components for the SPI & SPEI case, Journal of Hydrology 613 (2022) 128385. doi:10.1016/j.jhydrol.2022.128385.

[24] Q. Liu, S. Zhang, H. Zhang, Y. Bai, J. Zhang, Monitoring drought using composite drought indices based on remote sensing, Science of the Total Environment 711 (2020) 134585. doi:10.1016/j.scitotenv.2019.134585.

[25] L. Ma, Q. Huang, S. Huang, D. Liu, G. Leng, L. Wang, P. Li, Propagation dynamics and causes of hydrological drought in response to meteorological drought at seasonal timescales, Hydrology Research 53 (2021) 193–205. doi:10.2166/nh.2021.006.

[26] A. Barzkar, M. Najafzadeh, F. Homaei, Evaluation of drought events in various climatic conditions using data-driven models and a reliability-based probabilistic model, Natural Hazards 110 (2022) 1931–1952. doi:10.1007/s11069-021-05019-7.

[27] Y. Zhang, H. Yang, H. Cui, Q. Chen, Comparison of the ability of ARIMA, WNN and SVM models for drought forecasting in the San-

jiang Plain, China, Natural Resources Research 29 (2020) 1447–1464. doi:10.1007/s11053-019-09512-6.

[28] O. Ozan Evkaya, F. Sevinç Kurnaz, Forecasting drought using neural network approaches with transformed time series data, Journal of Applied Statistics 48 (2021) 2591–2606. doi:10.1080/02664763.2020.1867829.

[29] W. Almikaeel, L. Čubanová, A. Šoltész, Hydrological drought forecasting using machine learning—Gidra river case study, Water 14 (2022) 387. doi:10.3390/w14030387.

[30] M. Achite, M. Jehanzaib, N. Elshaboury, T.-W. Kim, Evaluation of machine learning techniques for hydrological drought modeling: A case study of the Wadi Ouahrane basin in Algeria, Water 14 (2022) 431. doi:10.3390/w14030431.

[31] Y. X. Tan, J. L. Ng, Y. F. Huang, A review on drought index forecasting and their modelling approaches, Archives of Computational Methods in Engineering (2022) 1–19. doi:10.1007/s11831-022-09828-2.

[32] A. Ahmadalipour, H. Moradkhani, M. C. Demirel, A comparative assessment of projected meteorological and hydrological droughts: Elucidating the role of temperature, Journal of Hydrology 553 (2017) 785–797. doi:10.1016/j.jhydrol.2017.08.047.

[33] K. Fung, Y. Huang, C. Koo, Y. Soh, Drought forecasting: A review of modelling approaches 2007–2017, Journal of Water and Climate Change 11 (2020) 771–799. doi:10.2166/wcc.2019.236.

[34] A. Hartmann, N. Goldscheider, T. Wagener, J. Lange, M. Weiler, Karst water resources in a changing world: Review of hydrological modeling approaches, Reviews of Geophysics 52 (2014) 218–242. doi:10.1002/2013RG000443.

[35] D. Ford, P. D. Williams, Karst hydrogeology and geomorphology, John Wiley & Sons, 2007.

[36] R. Lindgren, A. Dutton, S. Hovorka, S. Worthington, S. Painter, Conceptualization and simulation of the Edwards Aquifer, San Antonio Region, Texas: U.S., 2004.

[37] L. Shapley, A value for n-person games, Contributions to the Theory of Games (1953) 307–317.

[38] S. M. Lundberg, G. Erion, H. Chen, A. DeGrave, J. M. Prutkin, B. Nair, R. Katz, J. Himmelfarb, N. Bansal, S.-I. Lee, From local explanations to global understanding with explainable AI for trees, Nat. Mach. Intell. 2 (2020) 2522–5839. doi:10.1038/s42256-019-0138-9.

[39] A. Adadi, M. Berrada, Peeking inside the black-box: A survey on explainable artificial intelligence (XAI), IEEE Access 6 (2018) 52138–52160. doi:10.1109/ACCESS.2018.2870052.

[40] H. Başağaoğlu, D. Chakraborty, C. D. Lago, L. Gutierrez, M. A. Şahinli, M. Giacomoni, C. Furl, A. Mirchi, D. Moriasi, S. S. Şengör, A review on interpretable and explainable artificial intelligence in hydroclimatic applications, Water 14 (2022). doi:10.3390/w14081230.

[41] D. Rajsekhar, S. M. Gorelick, Increasing drought in Jordan: Climate change and cascading Syrian land-use impacts on reducing transboundary flow, Science Advances 3 (2017) e1700581. doi:10.1126/sciadv.1700581.

[42] S. I. Seneviratne, I. Lehner, J. Gurtz, A. J. Teuling, H. Lang, U. Moser, D. Grebner, L. Menzel, K. Schroff, T. Vitvar, M. Zappa, Swiss prealpine Rietholzbach research catchment and lysimeter: 32 year time series and 2003 drought event, Water Resources Research 48 (2012). doi:10.1029/2011WR011749.

[43] C. P. Petalas, K. N. Moutsopoulos, Hydrogeologic behavior of a complex and mature karst aquifer system under drought condition, Environmental Processes 6 (2019) 643–671. doi:10.1007/s40710-019-00382-x.

[44] E. Steiakakis, D. Vavadakis, M. Kritsotakis, K. Voudouris, C. Anagnostopoulou, Drought impacts on the freshwater potential of a karst aquifer in Crete, Greece, Environ Earth Sci 75 (2016) 507. doi:10.1007/s12665-016-5509-5.

[45] F. Fiorillo, F. M. Guadagno, Karst spring discharges analysis in relation

to drought periods, using the SPI, Water Resour. Manage. 24 (2010) 1867–1884. doi:10.1007/s11269-009-9528-9.

[46] G. Balacco, M. R. Alfio, M. D. Fidelibus, Groundwater drought analysis under data scarcity: The case of the Salento aquifer (Italy), Sustainability 14 (2022) 707. doi:10.3390/su14020707.

[47] V. Uddameri, S. Singaraju, E. Hernandez, Is standardized precipitation index (SPI) a useful indicator to forecast groundwater droughts? — insights from a karst aquifer, JAWRA Journal of the American Water Resources Association 55 (2019) 70–88. doi:10.1111/1752-1688.12698.

[48] B. F. Thomas, J. S. Famiglietti, Sustainable groundwater management in the arid southwestern US: Coachella Valley, California, Water Resources Management 29 (2015) 4411–4426. doi:10.1007/s11269-015-1067-y.

[49] L. A. Melsen, B. Guse, Hydrological drought simulations: How climate and model structure control parameter sensitivity, Water Resources Research 55 (2019) 10527–10547. doi:10.1029/2019WR025230.

[50] T. Devitt, A. Wright, D. Cannatella, D. Hillis, Species delimitation in endangered groundwater salamanders: Implications for aquifer management and biodiversity conservation, PNAS 116 (2019) 2624–2633. doi:10.1073/pnas.1815014116.

[51] EAHCP, Committee to Review the Edwards Aquifer Habitat Conservation Plan, Phase 3, 2018. doi:10.17226/25200.

[52] R. Maclay, Geology and hydrogeology of the Edwards Aquifer in the San Antonio Area, Texas: U.S., 1995.

[53] R. Green, F. Bertetti, B. Fratesi, G. Schindel, San Antonio Pool of the Edwards (Balcones Fault Zone) Aquifer, in: The Edwards Aquifer: The Past, Present, and Future of a Vital Water Resource, Geological Society of America, 2019. doi:10.1130/2019.1215(04).

[54] D. Chakraborty, H. Başağaoğlu, L. Gutierrez, A. Mirchi, Explainable ai reveals new hydroclimatic insights for ecosystem-centric groundwater management, Environmental Research Letters 16 (2021) 114024. doi:10.1088/1748-9326/ac2fde.

[55] A. M. Ukkola, M. G. De Kauwe, M. L. Roderick, G. Abramowitz, A. J. Pitman, Robust future changes in meteorological drought in CMIP6 projections despite uncertainty in precipitation, Geophysical Research Letters 47 (2020) e2020GL087820. doi:10.1029/2020GL087820.

[56] E. Peters, P. J. J. F. Torfs, H. A. J. van Lanen, G. Bier, Propagation of drought through groundwater—a new approach using linear reservoir theory, Hydrological Processes 17 (2003) 3023–3040. doi:10.1002/hyp.1274.

[57] A. C. Thomas, J. T. Reager, J. S. Famiglietti, M. Rodell, A GRACE-based water storage deficit approach for hydrological drought characterization, Geophysical Research Letters 41 (2014) 1537–1545. doi:10.1002/2014GL059323.

[58] K. Hayhoe, D. Cayan, C. B. Field, P. C. Frumhoff, E. P. Maurer, N. L. Miller, S. C. Moser, S. H. Schneider, K. N. Cahill, E. E. Cleland, L. Dale, R. Drapek, R. M. Hanemann, L. S. Kalkstein, J. Lenihan, C. K. Lunch, R. P. Neilson, S. C. Sheridan, , J. H. Vervillek, Emissions pathways, climate change, and impacts on California, PNAS 101 (2004) 12422–12427. doi:10.1073/pnas.0404500101.

[59] J. E. González, L. Ortiz, B. K. Smith, N. Devineni, B. Colle, J. F. Booth, A. Ravindranath, L. Rivera, R. Horton, K. Towey, Y. Kushnir, D. Manley, D. Bader, C. Rosenzweig, New York City panel on climate change 2019 report chapter 2: New methods for assessing extreme temperatures, heavy downpours, and drought, Annals of the New York Academy of Sciences 1439 (2019) 30–70. doi:10.1111/nyas.14007.

[60] S. Mukherjee, A. K. Mishra, M. Ashfaq, S.-C. Kao, Relative effect of anthropogenic warming and natural climate variability to changes in compound drought and heatwaves, Journal of Hydrology 605 (2022) 127396. doi:10.1016/j.jhydrol.2021.127396.

[61] A. Y. Sun, T. Bongiovanni, T. G. Caldwell, M. H. Young, Quantifying diffuse recharge at Camp Bullis, TX: Integrating soil water, evapo-

transpiration, and remote sensing. 2020 final report, submitted to the Edwards Aquifer Authority, 2020.

[62] L. Breiman, Random forests, Machine Learning 45 (2001) 5–32. doi:10.1023/A:1010933404324.

[63] T. Chen, C. Guestrin, XGBoost: A scalable tree boosting system, in: Proceedings of the 22nd ACM SIGKDD International Conference on Knowledge Discovery and Data Mining, 2016, pp. 785–794.

[64] P. Geurts, D. Ernst, L. Wehenkel, Extremely randomized trees, Mach Learn 63 (2006) 3–42. doi:10.1007/s10994-006-6226-1.

[65] D. Chakraborty, H. Başağaoğlu, J. Winterle, Interpretable vs. noninterpretable machine learning models for data-driven hydro-climatological process modeling, Expert Systems with Applications 170 (2021) 114498. doi:10.1016/j.eswa.2020.114498.

[66] D. Chakraborty, C. Ivan, P. Amero, M. Khan, C. Rodriguez-Aguayo, H. Başağaoğlu, G. Lopez-Berestein, Explainable artificial intelligence reveals novel insight into tumor microenvironment conditions linked with better prognosis in patients with breast cancer, Cancers 13 (2021). doi:10.3390/cancers13143450.

[67] D. Chakraborty, A. Alam, S. Chaudhuri, H. Başağaoğlu, T. Sulbaran, S. Langar, Scenario-based prediction of climate change impacts on build-

ing cooling energy consumption with explainable artificial intelligence, Applied Energy 291 (2021) 116807. doi:10.1016/j.apenergy.2021.116807.

[68] D. Chakraborty, H. Başağaoğlu, S. Alian, A. Mirchi, D. N. Moriasi, P. J. Starks, J. A. Verser, Multiscale extrapolative learning algorithm for predictive soil moisture modeling & applications, Expert Systems with Applications 213 (2023) 119056. doi:10.1016/j.eswa.2022.119056.

[69] N. S. Diffenbaugh, D. L. Swain, D. A. Touma, Anthropogenic warming has increased drought risk in California, PNAS 112 (2015) 3931–3936. doi:10.1073/pnas.1422385112.

[70] H.-F. Yeh, Spatiotemporal variation of the meteorological and groundwater droughts in central Taiwan, Front. Water 3 (2021) 636792. doi:10.3389/frwa.2021.636792.

[71] M. Ritorto, E. Screaton, J. Martin, P. J. Moore, Relative importance and chemical effects of diffuse and focused recharge in an eogenetic karst aquifer: an example from the unconfined upper Floridan aquifer, USA., Hydrogeol J 17 (2009) 1687–1698. doi:10.1007/s10040-009-0460-0.

[72] H. Başağaoğlu, L. Gergen, R. T. Green, Assessing the effects of epikarst on groundwater recharge and regional fast-flow pathways in a karstic aquifer via impulse-response functions, Journal of Hydrologic Engineering 20 (2015) 04015021. doi:10.1061/(ASCE)HE.1943-5584.0001183.

[73] Y. ben Cheng, H. bin Zhan, W. bin Yang, F. Bao, Deep soil water recharge response to precipitation in Mu Us Sandy Land of China, Water Science and Engineering 11 (2018) 139–146. doi:10.1016/j.wse.2018.07.007.

[74] R. Green, F. Bertetti, B. Fratesi, G. Schindel, San Antonio Pool of the Edwards (Balcones Fault Zone) aquifer, in: J. J. Sharp, R. Green, G. Schindel (Eds.), The Edwards Aquifer: The Past, Present, and Future of a Vital Water Resource: Geological Society of America Memoir, volume 215, 2019, p. 29–46. doi:10.1130/2019.1215(04).

[75] Mean temperature data from PRISM Climate Group, Oregon State University, (accessed 23 Apr 2023). URL: `https://prism.oregonstate.edu`.

[76] Annual precipitation data from PRISM Climate Group, Oregon State University, (accessed 13 Apr 2023). URL: `https://prism.oregonstate.edu`.